61701731

MECHANISM AND REACTION PATHWAYS OF CO_2 AND HCO_3^- PHOTOREDUCTION TO
HYDROCARBONS

Miss Duangthip Sattayamuk

A Thesis Submitted in Partial Fulfillment of the Requirements
for the Degree of Master of Engineering in Chemical Engineering
Department of Chemical Engineering
FACULTY OF ENGINEERING
Chulalongkorn University
Academic Year 2019
Copyright of Chulalongkorn University

กลไกและเส้นทางการเกิดปฏิกิริยารีดักชั่นเชิงแสงของคาร์บอนไดออกไซด์และไบคาร์บอเนตเป็น
สารประกอบไฮโดรคาร์บอน

น.ส.ดวงทิพย์ สัตยมุข

Thesis Title	MECHANISM AND REACTION PATHWAYS OF CO_2 AND HCO_3^- PHOTOREDUCTION TO HYDROCARBONS
By	Miss Duangthip Sattayamuk
Field of Study	Chemical Engineering
Thesis Advisor	Professor PIYASAN PRASERTHDAM, Ph.D.
Thesis Co Advisor	SUPAREAK PRASERTHDAM, Ph.D.
	Professor Oswaldo Rafael Nunez Sosa, Ph.D.

Accepted by the FACULTY OF ENGINEERING, Chulalongkorn University in Partial Fulfillment of the Requirement for the Master of Engineering

--- Dean of the FACULTY OF ENGINEERING

(Professor SUPOT TEACHAVORASINSKUN, D.Eng.)

THESIS COMMITTEE

--- Chairman

(CHALIDA KLAYSOM, Ph.D.)

--- Thesis Advisor

(Professor PIYASAN PRASERTHDAM, Ph.D.)

--- Thesis Co-Advisor

(SUPAREAK PRASERTHDAM, Ph.D.)

--- Thesis Co-Advisor

(Professor Oswaldo Rafael Nunez Sosa, Ph.D.)

--- Examiner

(Professor MUENDUEN PHISALAPHONG, Ph.D.)

--- External Examiner

(Assistant Professor Okorn Mekasuwandumrong, Ph.D.)

ดวงทิพย์ สัตยมุข : กลไกและเส้นทางการเกิดปฏิกิริยารีดักชั่นเชิงแสงของ
คาร์บอนไดออกไซด์และไบคาร์บอเนตเป็นสารประกอบไฮโดรคาร์บอน. (MECHANISM
AND REACTION PATHWAYS OF CO_2 AND HCO_3^- PHOTOREDUCTION TO
HYDROCARBONS) อ.ที่ปรึกษาหลัก : ศ. ดร.ปิยะสาร ประเสริฐธรรม, อ.ที่ปรึกษาร่วม :
ดร.ศุภฤกษ์ ประเสริฐธรรม,ศ. ดร.ออสวาโด ราฟาเอล นูวเนซ โซซา

ผลการทำปฏิกิริยาเชิงแสงของคาร์บอนไดออกไซด์และไบคาร์บอเนตพบว่าในสภาวะและ
เงื่อนไขที่ทำปฏิกิริยาเดียวกัน คาร์บอนมอนอกไซด์ผลิตได้มากที่สุดตามด้วยไฮโดรเจนและมีเทน
ตามลำดับ โดยที่การใช้ไบคาร์บอเนตเป็นสารตั้งต้นทำให้อัตราการเกิดปฏิกิริยาสามารถผลิตสาร
ไฮโดรคาร์บอนมากกว่าการใช้คาร์บอนไดออกไซด์ถึง 5 เท่า เนื่องจากค่าคงที่การดูดซับของ
คาร์บอนไดออกไซด์บนพื้นผิวของไททาเนียมไดออกไซด์มีค่าที่น้อยกว่า แบบจำลองทาง
จลนพลศาสตร์ของแลงเมียร์ถูกเลือกใช้สำหรับการศึกษากลไกของเกิดปฏิกิริยาภายใต้ค่าคงที่ของ
การดูดซับและค่าคงที่ของอัตราปฏิกิริยาบนพื้นผิวที่มีประจุต่างกัน พบว่าค่าคงที่การดูดซับมาก
ที่สุดเมื่อพื้นผิวไม่มีประจุ แต่ค่าคงที่ของอัตราปฏิกิริยามากที่สุดบนพื้นผิวที่เป็นประจุบวก สาร
ผลิตภัณฑ์ที่ถูกผลิตขึ้นจากปฏิกิริยานั้นเริ่มต้นมาจากการก่อตัวของอนุมูลอิสระประจุลบซึ่งเป็นขั้น
กำหนดของปฏิกิริยา แต่อย่างไรก็ตามระหว่างการทำปฏิกิริยาไบคาร์บอเนตอาจถูกดูดซับที่ช่องว่าง
ของออกซิเจนในตัวเร่งปฏิกิริยาแล้วก่อให้เกิดเส้นทางการเกิดปฏิกิริยาอื่น ซึ่งส่งผลให้
คาร์บอนมอนอกไซด์และไฮโดรเจนถูกผลิตมากขึ้นกว่าปกติ นอกจากนี้ผลของไอโซโทปตัวทำ
ละลายนั้นเหมือนกันในทุกการผลิตสารผลิตภัณฑ์หมายความว่าระหว่างการก่อตัวของอนุมูลอิสระ
มีการถ่ายโอนไฮโดรเจนหรือดิวเทอเรียมจากน้ำ การคู่ติดกันของผลึกชนิดอนาเทสและรูไทล์จาก
การปรับปรุงด้วยการโซนิคเคชันนอกจากจะทำให้อัตราปฏิกิริยาเพิ่มขึ้นแล้ว ยังเพิ่มความสามารถ
เลือกเกิดของมีเทนมากยิ่งขึ้นด้วย อีกทั้งยังช่วยลดเส้นทางการเกิดปฏิกิริยาอื่นจากช่องว่างของ
ออกซิเจน

สาขาวิชา	วิศวกรรมเคมี	ลายมือชื่อนิสิต ....
ปีการศึกษา	2562	ลายมือชื่อ อ.ที่ปรึกษาหลัก ....
		ลายมือชื่อ อ.ที่ปรึกษาร่วม ....
		ลายมือชื่อ อ.ที่ปรึกษาร่วม ....

6170173121 : MAJOR CHEMICAL ENGINEERING

Duangthip Sattayamuk : MECHANISM AND REACTION PATHWAYS OF CO_2 AND HCO_3^- PHOTOREDUCTION TO HYDROCARBONS. Advisor: Prof. PIYASAN PRASERTHDAM, Ph. D. Co-advisor: SUPAREAK PRASERTHDAM, Ph. D. ,Prof. Oswaldo Rafael Nunez Sosa, Ph.D.

CO_2/HCO_3^- photocatalytic reductions in water, using P25 Titanium dioxide, produce gas products at the order of the following rate: $CO>H_2>CH_4$, using bicarbonate as a substrate, reduction rates are ca. 5 times faster than using CO_2 due to the adsorption constant of CO_2 on the TiO_2 surface is smaller than the bicarbonate. Langmuir-Hinshelwood kinetic model was used to describe the mechanism; therefore, adsorption constant (K) and the rate of maximum substrate coverage (k) at different charges of P25-surface were readily obtained. The K constant of TiO_2-adduct formation favors no charge surface but k constant favors positive charge surface. Most of the products formed come from partitioning of the radical anion (TiO_2-$CO_2^{.-}$) in the rate-limiting step. However, the bicarbonate absorption at O_V promotes alternative pathways. This provides more CO and H_2 production. Solvent isotope effect (H_2O Vs. D_2O) is ca. 1.5. This means that during the radical anion formation in the transition state, there is H being transferred from water in the radical anion intermediate step. In addition, the collapse of anatase and rutile phases from sonication increases CH_4 production rate and selectivity due to improved charge separation that reduces alternative pathways.

Field of Study:	Chemical Engineering	Student's Signature	....
Academic Year:	2019	Advisor's Signature	....
		Co-advisor's Signature	....
		Co-advisor's Signature	....

ACKNOWLEDGEMENTS

จุฬาลงกรณ์มหาวิทยาลัย
CHULALONGKORN UNIVERSITY

TABLE OF CONTENTS

LIST OF TABLES

จุฬาลงกรณ์มหาวิทยาลัย

CHULALONGKORN UNIVERSITY

LIST OF FIGURES

CHAPTER I

INTRODUCTION

1.1 Introduction

CO_2 photoreduction is one of the photocatalytic processes that have gained much attention. This reaction is the capacity to transform the CO_2 to hydrocarbon. It uses solar energy for reaction activation, it is easily controlled and of low cost with also low pollution emission [1]. For effective use of reactions, understanding the reaction mechanism is important. There are several mechanisms proposed [2] but only a few studies focus on describing the rate limiting step. In general, there are two views of rate limiting step. First is substrate adsorption and product desorption [3]. Second is CO_2 and H_2O charge transfer of CO_2 reduction and H_2O oxidation on catalyst [4]. These rate limiting step have been proposed in pseudo-first order kinetic.

CO_2 is expected to be the adsorbed substrate on surface catalyst [5],[6]. However, when CO_2 gas is dissolved in the aqueous phase, bicarbonate ion (HCO_3^-) is the highest content of carbonate species [7]. Some research results show that hydrocarbon compounds can be produced from using HCO_3^- as the substrate in photoreduction [8]. Therefore, the mechanism of the HCO_3^- photoreduction process has not been studied in detail. In this study, mechanism and pathways of CO_2 or HCO_3^- photoreduction, have been described by using Langmuir-Hinshelwood approach. Therefore, kinetics LH parameters are used to explain the behavior of adsorbed molecules (K) on the catalyst surfaces and the rate at maximum adsorption (k) [9]. These constant values are associated to the ratedetermining step of the photoreduction. The proposed rate determining step is supported by using solvent isotope effect [10].

For photoreduction, the factors of catalyst type, pH, and others affect the photoreaction [11]. In the aqueous phase, the pH in solution is an important variable,

which influences the electron charge on the catalyst surface. The surface charge species affect the capability of activated reaction [12].

Many semiconductors are used in photocatalysis since an electron in the valence band can be excited to the conduction band by adsorbing photon from light irradiation [13]. Titanium dioxide (TiO_2) is commonly photocatalyst. Titanium dioxide has an energy bandgap potential to cover the redox potential of CO_2 photoreduction. Also, It is highly stable in reaction, available, and economical [14]. Commercial P-25 shows improved activity by the sonication method, [15] due to a synergy effect of the mixed two phases as compared to lower activity when the two phases are not mixed.

This research studied the mechanism and reaction pathway of CO_2 and HCO_3^- photoreduction to hydrocarbon products with the effect of pH in solution by using the Langmuir-Hinshelwood kinetic model. Solvent (H_2O Vs. D_2O) kinetic isotope effect has been measured for the reactor headspace gases detected. The pathways of reaction are identified by comparison of various product concentration ratios that are produced at the reaction time. In addition, sonicate pre-treatment method, in order to increase activity and selectivity performance, has been tested.

1.2 Objective

To study the mechanism and reaction pathways of CO_2 and HCO_3^- photoreduction to hydrocarbons in solution at different pH by using commercial TiO_2 (P-25) as photocatalyst. P-25 pre-treatment by sonication performance in rate and selectivity enhancements.

1.3 The scope of the research

1.3.1 CO_2 and HCO_3^- photocatalytic reduction to hydrocarbon products

The activity of the reaction was specified by hydrocarbons production rates from the CO_2 and HCO_3^- photocatalytic reduction with a cylindrical quartz reactor system that operates at 45°C, ambient pressure with UV-light irradiation for 4 hours.

1.3.2 Mechanism of CO_2 and HCO_3^- photocatalytic reduction

Langmuir-Hinshelwood kinetic model was used to explain the mechanism of CO_2 and HCO_3^- photocatalytic reduction. The kinetic model depends on the activity result of a reaction in each condition. The rate limiting step of reaction was confirmed by the solvent isotope effect value.

1.3.3 The Effect by pH of the reaction.

The pH of the solution that affects to surface charge of catalyst was varied by adding buffer NaH_2PO_4, 1 M of $NaOH$, and HCl solution before starting the experiment.

1.3.4 Effect of treatment on the catalyst for photoreduction.

Compare activity and selectivity between the original commercial TiO_2 and pre-treated TiO_2 by sonication method in the HCO_3^- photocatalytic reduction.

1.3.5   Characterization of the catalyst

The catalysts were characterized by using X-ray photoelectron spectroscopy (XPS), X-ray diffraction (XRD), UV-VIS Spectroscopy (UV-VIS), Scanning electron Microscope-Energy Dispersive X-ray Spectrometer (SEM-EDX), N_2 temperature-programmed desorption (BET) and Photoluminescence (PL).

1.4 Research methodology

```
┌─────────────────────────────────┐
│            Catalyst             │
└─────────────────────────────────┘
                │
                ▼
┌─────────────────────────────────┐
│      Degussa P25 (TiO$_2$)      │
└─────────────────────────────────┘
```

No Sonicated treatment

- Original catalyst

Sonicated treatment

- Disperse catalyst in water.
- Sonicate the catalyst in water for 30 minutes.
- Dry in oven at 110°C

Surface charge of catalyst

- Varying pH 5.2-7.2

Photocatalytic activity test

- Cylindrical quartz reactor
- Temperature = 45 °C
- Pressure = 1 atm

Characterized

- XPS
- XRD
- UV-vis
- SEM-EDX
- BET
- PL

Discussion

Conclusion

CHAPTER II

BACKGROUND AND LITERATURE REVIEWS

2.1 Solar energy

The industries in the world have increased that resulting in an increase in demand for energy every year, in which the energy sources are limited and rapidly disappear. While the energy consumed has caused pollution to the environment, such as the main greenhouse gas CO_2 emission, causing global warming to increase from 25 billion tons in 2000 to 35 billion tons in 2017 [16]. Therefore, much research in finding a solution to reduce critical effects and renewable energy is constantly developed. One method is using solar energy, which is unlimited in irradiation energy (50,000 EJ on the earth's surface) and does not emit pollution while using it as an energy source. Solar energy is radiation and the heat from the sun, which has been developed to be combined with technologies for various benefits, such as heating, electrical energy conversion, salt production, and photocatalytic reactions, etc. [17].

Photocatalytic reduction of the greenhouses gas to produce hydrocarbon products is a promising process which can reduce greenhouse gas emission from human activity. Photocatalytic CO_2 reduction is one of the reactions that can reduce the principal gas of global warming.

2.2 Photocatalysts

Generally, photocatalysts are the semiconductor that consists in compounds in between metal and non-metal elements, so this material has electrical conductivity between the conductor and insulator [18]. The semiconductor consists of a valence band (VB) and a conduction band (CB) at different potential energy levels, the gap between the energy level of CB and VB is the energy bandgap (EG). So that, photocatalyst catalyzes reaction by absorbing photons from energy light irradiation to

to produce an excited-state, a transient step of the electron-hole pair process (e^-/h^+) [19].

$$\text{Photocatalyst} + hv\ (\geq \text{EG}) \longrightarrow e^-_{(CB)} + h^+_{(VB)} \qquad\qquad \text{Eq. 1}$$
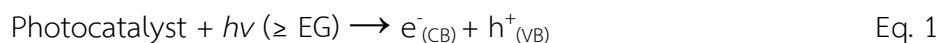
The electron-hole pair process is the excited-electron transfer from VB to CB that makes the conduction band to have an excess electron (e^-); therefore, more negative potential to reduce the adsorbed reactant. In contrast, the valence band creates an empty electron state or a hole (h^+) to be more positive potential and induce the absorbed reactant in the system to be oxidized [20].

The redox reaction on photocatalyst with considered species compound in the system depends on the redox potential energy of oxidized species agent (E_1) and reduced species agent (E_2), the potential energy level of the conduction band (CB) and valence band (VB). When the electron-hole pair process occurs, as shown in Figure 1, the conduction band that has more negative potential than the redox potential energy of oxidized species agent will reduce electron to oxidized species agent (Red_1 to OX_1) as the reduction reaction. At the same time, the valence band that has more positive potential than the redox potential energy of reduced species agent will oxidize electron to reduced species agent (Red_2 to OX_2) as the reduction reaction [21].
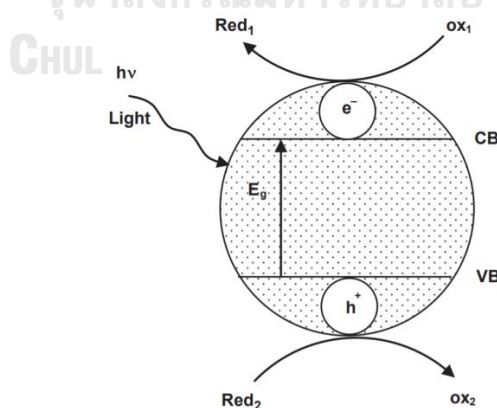
Figure 1 Schematic illustration of the photoexcitation process in a semiconductor particle. OX_1, Red_1, OX_2, and Red_2, represent, respectively, the oxidized and the reduced species of two different redox couples.

Nevertheless, the transient step of the electron-hole pair process can be inhibited and reduce activity when an electron-hole recombination process occurs. The electron-hole recombination is excited-electron from the valence band to conduction band do not has enough activate energy. It will go back to hole in the valence band [22].

$$e^-_{(CB)} + h^+_{(VB)} \longrightarrow \text{Energy (Recombination)} \qquad \text{Eq. 2}$$

2.3 Titanium dioxide

Titanium dioxide (TiO_2) is one of the semiconductors widely used in photoreaction for reducing contaminants in water sources [23] and greenhouse gases in the atmosphere [24]. The reaction is not violent and does not produce toxic substances [25].

Molecular weight is 79.9 g.mol^{-1}, the boiling point is 1830 ^{o}C. Titanium dioxide is an n-type semiconductor compound of a Titanium transition metal bond with Oxygen's around. There is a crystallography phase with different energy bandgaps such as anatase in the tetragonal system (EG = 3.2 eV), rutile in the tetragonal system (EG = 3.0 eV), and brookite in the orthorhombic system (EG = 2.8 eV) as shown in Figure 2. Due to this difference of crystal systems which these different distances between Ti-Ti or Ti-O atoms lead to unequal energy levels [26], [27].
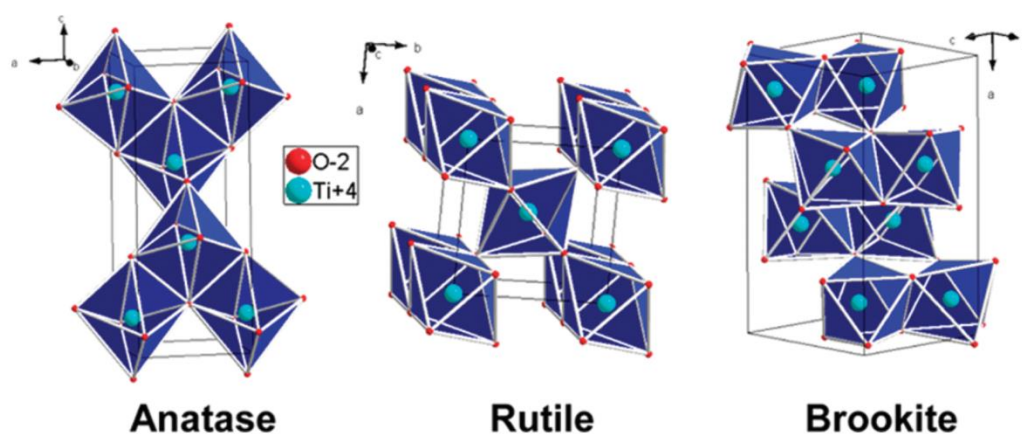
Figure 2 Representations of the TiO2 anatase, rutile, and brookite forms.

Table 1 Crystal structure properties for anatase, rutile and brookite phase of TiO_2

Property	Anatase	Rutile	Brookite
Crystal bulk structure	Tetragonal	Tetragonal	Orthorhombic
Atoms per unit call [Z]	4	2	8
Crystal size (nm)	<11	>35	11-35
Lattice parameter (nm)	a = b = 0.3785, c = 0.9514	a = b = 0.4594, c = 0.2959	a = c = 0.5436, b = 0.9166
Space group	D_{4h}^{19}- I4$_1$/amd	D_{4h}^{19}- P4$_2$/amd	D_{2h}^{15}- Pbca
Unit call volume (nm^3)	0.1363	0.0624	NA
Density ($g.cm^{-3}$)	3.83	4.24	4.17
Band gap (eV)	3.26	3.05	NA
Hardness (Mohs)	5.5-6	6-6.5	5.5-6

From properties Table 1 [28], the anatase phase of titanium dioxide has an energy band gap at 3.26 eV that can be excited by absorbing photon under UV irradiation wavelength in 384 nm. In comparison, the rutile phase has an energy band gap at 3.05 eV that can be excited by absorbing photon under visible light wavelength at 410 nm. The rutile can be transferred electron easier than the anatase because of the lower energy bandgap [29].

Huilei Zhao., et al. (2013) [30] used pure anatase, rutile and brookite phase of titanium dioxide in CO_2 photoreduction. The production rate of carbon monoxide (CO) is 12 μmol.g-^{1}.h^{-1} (pure anatase phase), 0.75 μmol.g^{-1}.h^{-1} (pure brookite phase). Moreover, the best activity was obtained from the mixing phase of the 75% anatase phase with 25% brookite phase.

Wenzhang Fang., et al. (2017) [31] investigated the activity from varying ratio anatase and rutile phase of TiO_2 by reducing the anatase phase in TiO_2 photocatalysts with H_2 thermal treatment. For the production rate of CO_2 photoreduction to CO, the

pure rutile phase had 0.5 μmol.g^{-1}.h^{-1} while mixing of 26% anatase and 74% rutile phases had 0.8 μmol.g^{-1}.h^{-1}. The selectivity of methane production was increased as increasing in the anatase phase, but the CO production rate was decreased.

2.4 Possible photoreduction mechanism and pathways

Photocatalytic CO_2 reduction mechanism in the aqueous phase has been studied and anticipated the possible pathway. The photoreduction begins by photocatalyst absorb photon from light irradiation to be excited-state. The catalyst will enter the transient step of generating the electron-hole pair (e^-/h^+) and start a redox reaction. The electron (e^-) in the valence band is excited to conduction band while the valence band generates the hole (h^+).

Photocatalyst + hv (>EG) $\longrightarrow$ Excited photocatalyst (e^-_{CB} + h^+_{VB})　　Eq. 3

The hole in the valence band will act as a reducing agent and induce H_2O on catalyst surface to oxidize electron from H_2O with oxidation reaction. The oxidized H_2O will break its bond to be protons (H^+) and hydroxide ion (OH^-). The protons will oxidize the electron in the conduction band to be hydrogen radical ($\overset{\bullet}{H}$) that is an indispensable hydrogen atom source to produce hydrocarbon products. At the same time, the hydroxide ion will continue to reduce electron to hole in the conduction band and produce hydroxyl radical ($\overset{\bullet}{OH}$) [32].

H_2O + h^+_{VB} $\longrightarrow$ H^+ + OH^-　　　　　　　　　　Eq. 4

H^+ + e^-_{CB} $\longrightarrow$ $\overset{\bullet}{H}$　　　　　　　　　　　　　　Eq. 5

OH^- + h^+_{VB} $\longrightarrow$ $\overset{\bullet}{OH}$　　　　　　　　　　　　Eq. 6

For producing hydrocarbon from photocatalytic CO_2 reduction, the dissolved carbon dioxide in the H_2O aqueous solution is a carbon atom source to produce hydrocarbon products in photoreduction. The carbon dioxide as oxidized species agent adsorbs on the active site of an exciting photocatalyst to be oxidized electron from the conduction band. After that, carbon dioxide form $\overset{\bullet}{CO_2^-}$ radical anion (Eq. 10) and

continuously attract hydrogen radical to form carbon monoxide (CO) as first hydrocarbon product and hydroxide ion (OH^-) (Eq. 8). Produced carbon monoxide on surface continuously reduces electrons to form $\overset{\bullet}{C}O^-$ radical anion species (Eq. 9) and attract with hydrogen radical to form first carbon radical ($\overset{\bullet}{C}$) (Eq. 10) that will bind with hydrogen radicals until form hydrocarbon molecule (Eq. 12- 13) . Methane and methanol are hydrocarbon products of photoreduction that have a different form of $\overset{\bullet}{C}H_3$ with $\overset{\bullet}{H}$ radical (Eq. 15) and $\overset{\bullet}{O}H$ radical (Eq. 16) [33].

$$CO_2 + e^-_{CB} \longrightarrow \overset{\bullet}{C}O_2^- \qquad\qquad \text{Eq. 7}$$

$$\overset{\bullet}{C}O_2^- + \overset{\bullet}{H} \longrightarrow CO + OH^- \qquad\qquad \text{Eq. 8}$$

$$CO + e^-_{CB} \longrightarrow \overset{\bullet}{C}O^- \qquad\qquad \text{Eq. 9}$$

$$\overset{\bullet}{C}O^- + \overset{\bullet}{H} \longrightarrow \overset{\bullet}{C} + OH^- \qquad\qquad \text{Eq. 10}$$

$$\overset{\bullet}{C} + 3\overset{\bullet}{H} \longrightarrow \overset{\bullet}{C}H_3 \qquad\qquad \text{Eq. 11}$$

$$\overset{\bullet}{C}H_3 + \overset{\bullet}{H} \longrightarrow CH_4 \qquad\qquad \text{Eq. 12}$$

$$\overset{\bullet}{C}H_3 + \overset{\bullet}{O}H \longrightarrow CH_3OH \qquad\qquad \text{Eq. 13}$$

The two hydroxide ions that produced from $\overset{\bullet}{C}O_2^-$ radical anion and $\overset{\bullet}{C}O^-$ radical anion bind with hydrogen radicals (Eq. 7-9), can be induced and oxidize electron by the hole in valence band with oxidation reaction to form H_2O [34].

$$2OH^- + 2h^+_{VB} \longrightarrow 2\overset{\bullet}{O}H \qquad\qquad \text{Eq. 14}$$

$$2\overset{\bullet}{O}H + 2\overset{\bullet}{H} \longrightarrow 2H_2O \qquad\qquad \text{Eq. 15}$$

The photoreduction of carbon dioxide can produce various hydrocarbon products. These products Redox potential or thermodynamic potential (E_0) in standard conditions at pH = 7, temperature 25°C and pressure 1 atm are shown in Table 2. In order to photoreduction to occur, semiconductor catalyst should have conduction band redox potential more negative than CO_2 E_0 and valence band E_0 more positive than H_2O E_0 at the reaction pH. Titanium dioxide is one of catalyst that could comply with the Eo reduction requirement. [35]

Table 2 Thermodynamic potential (E_0) of CO_2 photoreduction.

Hydrocarbon Product	Chemical Reaction	Thermodynamic potential (E_0), NHE at pH 7
	$CO_{2(g)} + e^- \longrightarrow \overset{\bullet}{C}O_{2\ (aq)}^-$	-1.99
	$CO_{2(aq)} + e^- \longrightarrow \overset{\bullet}{C}O_{2\ (aq)}^-$	-1.90
Formic acid	$CO_{2(aq)} + 2H^+_{(aq)} + 2e^- \longrightarrow HCOOH_{(aq)}$	-0.61
Carbon monoxide	$CO_{2(aq)} + 2H^+_{(aq)} + 2e^- \longrightarrow CO_{(g)} + H_2O_{(l)}$	-0.52
Formaldehyde	$CO_{2(aq)} + 4H^+_{(aq)} + 4e^- \longrightarrow H_2C(OH)_{2(aq)} + H_2O_{(l)}$	-0.49
Methanol	$CO_{2(aq)} + 6H^+_{(aq)} + 6e^- \longrightarrow CH_3OH_{(aq)} + H_2O_{(l)}$	-0.38
Methane	$CO_{2(aq)} + 8H^+_{(aq)} + 8e^- \longrightarrow CH_{4\ (g)} + H_2O_{(l)}$	-0.34

2.5 Photocatalytic reduction with Bicarbonate ions

Bicarbonate ion (HCO_3^-) is one of the carbon sources for photocatalytic reduction. It is a form of dissolved carbon dioxide in water and formed at the beginning of the CO_2 photoreduction pathway. When carbon dioxide dissolves in water by a dissolution process, the carbon dioxide reacts with water to form carbonic acid (H_2CO_3), hydrogen ions (H^+) and bicarbonate ions (HCO_3^-) as Eq. 16-18 [36].

$$CO_{2(g)} \text{ (atmospheric)} \longrightarrow CO_{2(aq)} \text{ (dissolved)} \qquad \text{Eq. 16}$$

$$CO_{2(aq)} + H_2O_{(l)} \longrightarrow H_2CO_{3(aq)} \qquad \text{Eq. 17}$$

$$H_2CO_{3(aq)} \longrightarrow H^+ + HCO_{3\ (aq)}^- \qquad \text{Eq. 18}$$
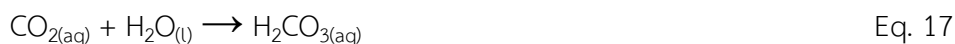
The bicarbonate (HCO_3^-), carbon monoxide (CO), and methane (CH_4) can be produced by CO_2 photoreduction as Eq. 22-28. At the beginning of the CO_2 photoreduction pathway, the adsorbed carbon dioxide on excited active site is reduced to form a $\overset{\bullet}{C}O_2^-$ radical anion. After that, the $\overset{\bullet}{C}O_2^-$ radical anion can attract with

hydroxide ion ($\dot{O}H$) to form bicarbonate (HCO_3^-). The bicarbonate can be used as an initial carbon substrate to produce hydrocarbon products [37].

$$H_2O + h^+_{VB} \longrightarrow H^+ + \dot{O}H \qquad \text{Eq. 19}$$

$$CO_2 + e^-_{CB} \longrightarrow \dot{C}O_2^- \qquad \text{Eq. 20}$$

$$\dot{C}O_2^- + \dot{O}H \longrightarrow HCO_3^- \qquad \text{Eq. 21}$$

$$\dot{C}O_2^- + H^+ + e^- \longrightarrow CO + OH^- \qquad \text{Eq. 22}$$

$$\dot{C}O_2^- + \dot{C}O_2^- \longrightarrow CO + \dot{C}O_3^{2-} \qquad \text{Eq. 23}$$

$$\dot{C}O_3^{2-} + v_O \text{ (oxygen vacancy)} \longrightarrow CO \qquad \text{Eq. 24}$$

$$CO, HCO_3^-, HCOOH + e^-_{CB} \longrightarrow \dot{C}_{(ads)} + 3\,\dot{H} \longrightarrow \dot{C}H_3 + \dot{H} \longrightarrow CH_4 \qquad \text{Eq. 25}$$
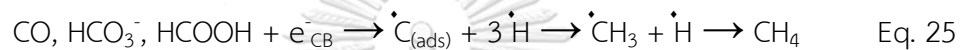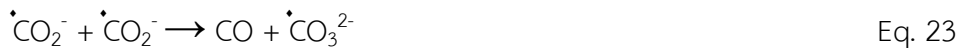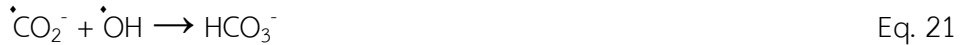
Furthermore, bicarbonate is one of the electron scavengers that can trap electrons and reduce electron from the conduction band to form formate ion (HCO_2^-) as Eq. 26. Formed formate ion is trapped with hydroxide radical ($\dot{O}H$) to form hydroxide ion ($\dot{C}O_2^-$) (Eq. 27) [38] that can continually bind with another radical to produce hydrocarbon product. This process like CO_2 photoreduction pathway as Eq. 11-16.

$$HCO_3^- + 2e^-_{CB} + 2H^+ \longrightarrow HCO_2^- + H_2O \qquad \text{Eq. 26}$$

$$HCO_2^- + \dot{O}H \longrightarrow \dot{C}O_2^- + H_2O \qquad \text{Eq. 27}$$

2.6 Photocatalytic reduction and pH dependency

The pH of the solution is important variables influencing the photocatalytic reduction process in the aqueous phase. For titanium dioxide surface, pH resulting in charge surface is changed as acid-base equilibrium reaction (Eq. 28-29) [12]. The pH influencing the charged surface of the catalyst has been identified by using the isoelectric point (pH_{IEP}) or the point of zero charges (pH_{PZC}), which is pH of no electrical charge on the only external surface or both internal and external surface of catalyst particle [39]. The pH_{PZC} is estimated with averaged pK_a of pure positive and negative charge surface condition (pK_{a1} = 4.5, pK_{a2} = 8), The estimated pH_{PZC} of Degussa P25 is 6.2, which the titanium dioxide show no charge or neutral charge surface [12].

$$Ti\text{-}OH + H^+(pK_{a1}) \longrightarrow Ti\text{-}OH_2^+ \hspace{3cm} \text{Eq. 28}$$

$$Ti\text{-}OH + OH^-(pK_{a2}) \longrightarrow Ti\text{-}O^- \hspace{3cm} \text{Eq. 29}$$
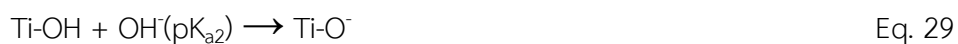
Therefore, the titanium dioxide in pH 6.2 aqueous solution is hydrated with H_2O to have a hydroxyl group on the surface (Ti-OH) as a neutral charge surface [40]. Lower pH<6.2 or acidic condition contributes to a higher amount of hydrogen ion (H^+) that protonated to an oxygen atom in the hydroxyl group to form (Ti-OH_2^+) as a positive charge surface. High pH>6.2 contributes to a higher amount of hydroxide ion (OH^-) that attracts the hydrogen atom in hydroxyl group or deprotonated to form (Ti-O^-) as negative charge surface as shown in Figure 3 [41],[42].
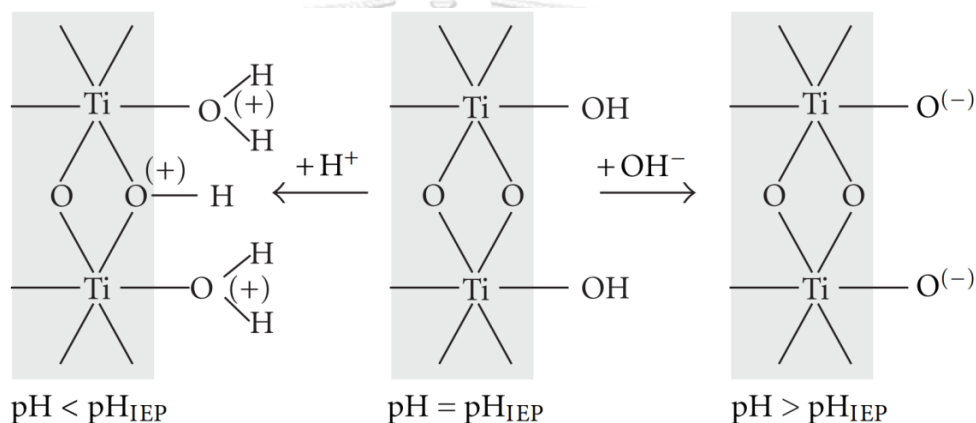
Figure 3 Simplified scheme of the protonation and deprotonation of hydroxylated TiO_2 surface [43].

The charge surface species affects the absorption and activity of reactants on the catalyst surface. The reactants are adsorbed better when reactant charge is opposite with the charged surface. Furthermore, the appropriate charge surface species of the catalyst also increases the electron transfer efficiency in the transient state and the selectivity of some products [44]. In the case of CO_2 photoreduction on Fe_3S_4 at pH 4.5-9 solution, the highest production rate of methanol is obtained at pH 6.5 since this condition increases CO_2 solubility in the solvent [45]. For high-pressure CO_2 photoreduction to hydrogen, carbon monoxide and formic acid products on Degussa P25 (TiO_2) in basic solution at pH 7.5 to 14, the strong basic solution obtained by

adding scavenger that increases CO_2 solubility (pH 14), yields more productivity and selectivity of hydrogen and formic acid [46]. Low pH condition (pH 1-3) results in more methane production from CO_2 photoreduction with Pd/TiO_2 because solution at pH lower than 6 has more amount of hydrogen ion (H^+), a hydrogen atom source for methane formation [47].

2.7 Langmuir–Hinshelwood mechanism

Langmuir-Hinshelwood mechanism, suggested by Irving Langmuir (1921) and developed by Cyril Hinshelwood (1926) is the process that has two reactant molecules adsorb on near the site of the catalyst surface, and these two adsorbed molecules may interact or recombine with each other [5]. Therefore, this process is suitable for the solid-liquid interface reaction or the heterogeneous catalytic [48]. This mechanism can be extended using Langmuir-Hinshelwood kinetics (LH) that is the common kinetics for explaining the reaction mechanism on the heterogeneous surface of the catalyst. The Langmuir-Hinshelwood kinetic model (LH-kinetics) is shown as follows:

$$r = -\frac{d[C]}{dt} = \frac{kK[C]}{1+K[C]} \qquad \text{Eq. 30}$$

Where r is the rate of reaction that is the function of reactant concentration at any time reaction (C), the reaction time (t), the limiting reaction rate constant at maximum reactant concentration (k) and the absorption coefficient of the reactant on the catalyst (K). Eq. 30 is approximated to first-order kinetics, if 1 > K[C] in Eq. 30. The LH kinetics is usually approximated to be the first-order kinetics for sustain $K[C] \ll 1$ condition and approximated to be the zero-order kinetics for sustain $K[C_0] \gg 1$ condition. Furthermore, in the cases of reactant adsorption, $K[C] \ll 1$ is reactant molecules that have low adsorption, and $K[C] \gg 1$ is reactant molecules having high adsorption [49].

$$r_0 = \frac{kK[C_0]}{1+K[C_0]} \qquad \text{Eq. 31}$$

$$\frac{1}{r_0} = \frac{1}{k} + \frac{1}{kKC_0} \qquad \text{Eq. 32}$$

The reaction rate constant (k) and the adsorption coefficient (K) can be estimated from using Eq. 30 in terms of initial reaction rate (r_0) as a function of initial reactant concentration (C_0) as Eq. 31 with converting the equation form to a linear equation form as Eq. 32 [9].

I. Poulios et al. [48] In the case of photocatalytic degradation on TiO_2 (P25) in aqueous solution, this reaction was described by using the modified Langmuir–Hinshelwood model to accommodate reactions occurring at a solid-liquid interface. LH equation Eq. 30 was used in terms of initial rate (r_0) and the equilibrium bulk-solute concentration (C_{eq}) and modified equation to Eq. 33 for linearity plotted as follows:

$$\frac{C_{eq}}{r_0} = \frac{1}{kK} + \frac{C_{eq}}{k} \qquad\qquad \text{Eq .33}$$

From experiments, the concentration of substrate decreased with reaction time, and the initial rate was obtained from each condition. The K and k constants can be deduced from the slope and the intersection of the trend line from the r_0/C_{eq} vs C_{eq} plot (Figure 4).
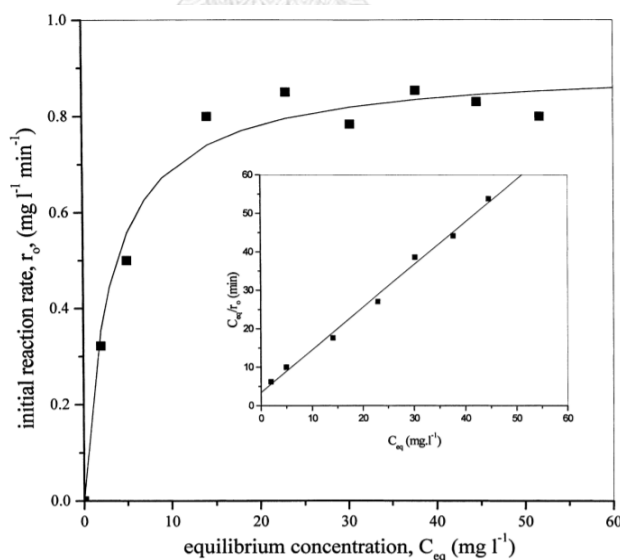
Figure 4 Plot of r_0 vs C_{eq} at different initial concentrations with 1 gl^{-1} TiO_2 P-25. Inset: linear transform of C_{eq}/r_0 vs C_{eq} according to Eq. 33.

2.8 Kinetic solvent isotope effects

The kinetic isotope effect (KIEs) is an effect in which the reaction rate is changed by the isotope substrate replacing. The isotope effect is used to describe reaction kinetics, identifying reaction mechanism by determining its rate limiting steps (RLS), Change of isotope substrate makes the equilibrium of the reaction different. Isotope is the same element atoms which have the same ato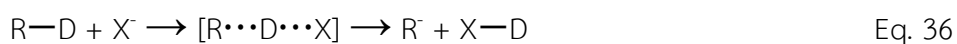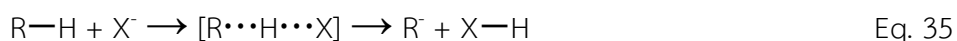mic number but the different mass number or the different neutron number. For example, for studying the kinetic isotope effect, H_2O solvent with the one mass number of hydrogen atoms (^1H) is changed to D_2O solvent (Deuterium) with the two mass number of hydrogen atoms (^2H). Reaction rates are measured using H_2O and D_2O under the same reaction condition.

$$KIEs = k_H/k_D \qquad\qquad\qquad \text{Eq. 34}$$

KIEs is investigated by comparing the ratio of the rate constants that depend on the different reaction rate results. The KIEs of deuterium affection is obtained from comparing the ratio of the rate constants (k_H/k_D). The different mass number percentage between the lighter and the heavier mass substrate affects how large the KIEs is. Generally, the KIEs of deuterium can yield k_H/k_D values of low effect ca. 1 to a high value of ca. 7 depending on the reaction. KIEs value indicates the isotope effect type.

2.8.1 Primary kinetic isotope effects

Primary kinetic isotope effects (PKIEs) is the large affection which bond of the substrate (R-H) and its isotope substrate (R-D) is broken in the rate limiting step of a reaction. For example, consider a reaction R-H as substrate reacts with X^- to produce X-H as shown in Eq. 35 and R-H as substrate is changed to R-D as its isotope or deuterium substrate as Eq. 36

$$R{-}H + X^- \longrightarrow [R{\cdots}H{\cdots}X] \longrightarrow R^- + X{-}H \qquad\qquad \text{Eq. 35}$$

$$R{-}D + X^- \longrightarrow [R{\cdots}D{\cdots}X] \longrightarrow R^- + X{-}D \qquad\qquad \text{Eq. 36}$$

After the hydrogen (R-H) is changed to deuterium (R-D) in the considered reaction, cleavage of R-D substrate bond decreases the overall reaction rate during the rate limiting step and gave the KIEs or $k_H/k_D > 1$.

If the KIEs = 1 then the step: $R{-}H + X^- \longrightarrow [R{\cdots}H{\cdots}X]$ is not the RLS.

If the KIEs > 1 then the step: $[R{\cdots}H{\cdots}X] \longrightarrow R^- + X{-}H$ is the RLS.

$L = H$ or T $k_H/k_T = 1.3$

$L = H$ or D $k_H/k_D = 3.7$
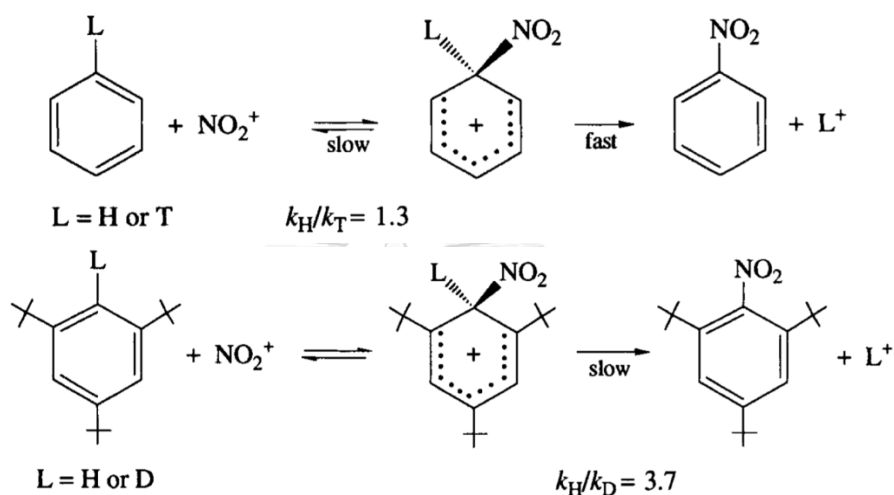
Figure 5 Primary kinetic isotope effect from aromatic electrophilic substitution in the nitration of benzene [50].

2.8.2 Secondary kinetic isotope effects

Secondary kinetic isotope effects (SKIEs) are the small affection which KIEs is around 1 **[51]**. The isotope bond is not cleaved during the reaction, but its bond is effected by being near to the actual reaction centre. The difference distances between the isotope and the reaction centre positions. These come in three forms of secondary isotope effect: **α**-SKIEs, **β**-SKIEs, and **γ**-SKIEs effects. The small effects are caused by the activation energy changing in RLS that effect to hybridization and hyperconjugation on the energy of isotope bond.

For **α**-SKIEs, there are two types of **α**-SKIEs. The normal **α**-SKIEs ($k_H/k_D \geq 1$), the reaction rate is reduced when the hybridization degree of the reaction centre in the transition state is lower than the reaction centre in RLS (sp^3 to sp^2, sp^2 to sp^1). On

the other hand, the inverse α-SKIEs ($k_H/k_D \leq 1$) increase the reaction rate when the hybridization degree of the reaction centre in the transition state is higher than RLS (sp to sp^2, sp^2 to sp^3) [52].
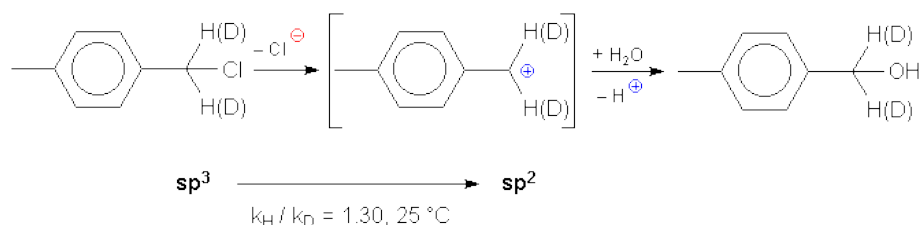
Figure 6 The normal secondary isotope effect of α-phenylmethyl chloride **[53]**.
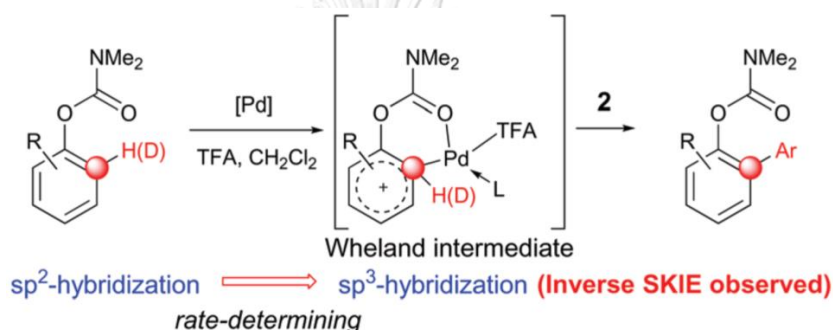
Figure 7 The inverse secondary isotope effect of Wheland intermediate [54].

2.8.3 Heavy atom isotope effects

The Heavy atom isotope effects have KIEs around 1. The small isotope effect occurs by slightly different from the mass number between the substrate such as $^{14}N/^{15}N$, $^{20}Ne/^{21}Ne$ and $^{35}Cl/^{37}Cl$ etc.

2.8.4 Solvent isotopic effect

The solvent effect in the reaction is like the primary isotope effect where the solvent can act as the substrate (reaction has excess substrate). The reaction is effected by exchanging isotope solvent like H_2O to D_2O. The heavier mass atom of deuterium may change positions in the molecule to be the new molecule that can react in RLS. The solvent interactions may change the energy in the transition state and result in secondary isotope effects.

Oswaldo Núñez et al. [10] studied the solvent isotope effect of glucose photooxidation with large solvent (H_2O vs D_2O) on Bi_2WO_6 semiconductor. From experiment result, the large solvent isotope effects gave $k_{H2O}/k_{D2O} = 7.8$ and 6.8. These values come from the equilibrium dissociation of L_2O ionization to L^+ and OL^-, (L_2O, L= H or D). The reaction rate is faster when L^+ concentration ($[L^+]$) increase in acidic condition. Therefore, the rate limiting step is the one e^- reduction of H^+ at Bi_2WO_6 conduction band. At the conduction band of catalyst (CB), the reduction of O_2 to O_2^{--} and H^+ to H_2 by using Bi_2WO_6 as cathode gave the small solvent isotope effect of KIEs 2.4 and 1.9, respectively.

2.9 Literature reviews

T. Inoue et al., [55] studied the carbon dioxide photocatalytic reduction in aqueous suspensions of some semiconductor powers (TiO_2, ZnO, CdS, GaP, SiC, and WO_3). This reaction could reduce CO_2 to produce hydrocarbons such as methanol, formaldehyde, formic acid in the aqueous sample, and methane in the gaseous sample. The best semiconductor catalyst for this report was SiC, which had conduction band potential near CO_2 photoreduction to hydrocarbon potential.

Yasar N. Kavil et al., [56] used Cu-C/TiO_2 as photocatalyst in the CO_2 photocatalytic system. The catalyst was suspended with a controlled pH solution and stirred in the Pyrex glass reactor that was connected with the CO_2 cylinder. Before started reaction, the solution with catalyst was purged with super high purity CO_2 for 30 minutes until saturated in solution and turn off CO_2 cylinder to stop purging. The reactor must be completely closed to avoid the outer contact. The UV-lamp was turned on and syringe was used to take samples. The maximum of methanol yield was 2593 $\mu molg_{cat}^{-1}$ after 5 hours.

K. Koci et al., [57] studied wavelength effect to CO_2 photoreduction on Ag/TiO_2 under irradiation by different lamps in the wavelength range 254-400 nm. The main

products, methane and methanol were obtained in higher yielods with UV light (254 nm).

K. Wooyul et al. , [58] found that pH affects CO_2 photoreduction. Photoreduction activity increases at low pH, to yield the highest methane production due to the excess of protons around the active site that could be used for CO_2 reduction. At high pH ca. 11, CO_2 solubility increases to form an intermediate of carbonate that could produce solar fuel, but it not significant CO_2 reduction probably due to the lack of protons in solution.

Tai-Sing Wu et al., [59] found that Ultraviolet light irradiation on CeO_2 catalysts could increase the photocatalytic activity of the catalyst and reduce electron-hole recombination. The carbon monoxide conversion was increased as the increase of active site Ce^{3+} on the catalyst surface and oxygen vacancy by UV-light irradiation time (254 nm, UV-C). Therefore, the increased activity is presented as experimental evidence to confirmed that UV-light irradiation-induced reduction Ce^{4+} ions to Ce^{3+} ions and created oxygen vacancies.

Terihisa Ohno et al., [60] has shown using TEM photographs and electron diffraction patterns, Degussa P25 (TiO_2 powder) consists of 75% anatase and 25% rutile phase that were separated. When P25 reacted in photoreaction, the anatase and rutile were not reacted together, yielded low activity. Nevertheless, anatase and rutile phase could co-work by using previous HF treatment, which dispersed both phases of the TiO_2 powders in water or 10% HF solution and sonicated for 30 min. After treatment, the coupling of both phases in TiO_2 provides the higher activity of naphthalene photooxidation.

CHAPTER III

EXPERIMENTAL

This chapter describes the details of materials and chemicals, reaction measurement, preparation, analysis result equipment, and characterization.

3.1 Materials and Chemicals

Table 3 List of materials and chemicals, reactant solution, catalyst, calibration standard, and equipment gas supply.

Chemical Name	Formula	Purity (%)	Suppliers
Degussa (P25)	TiO_2	-	Aeoxide
Sodium hydrogen carbonate	$NaHCO_3$	99.0 %	Fluka Chemika
Sodium phosphate	NaH_2PO_4	99.0 %	ACROS ORGANICS
Sodium hydroxide	$NaOH$	99.0 %	EMSURE
Hydrochloric acid fuming	HCl	37 %	EMSURE
Phenol crystallized	C_6H_5OH	99.0 %	Panreac
Deuterium oxide	D_2O	99.9 %	Cambridge Isotope Laboratories, Inc.
Dimethyl sulfoxide, DMSO	C_2H_6OS	99.5 %	Sigma-Aldrich
Carbon dioxide	CO_2	99.99 %	Linde
Methane	CH_4	99.99 %	Linde
Carbon monoxide	CO	99.99 %	BOC GASES
Hydrogen	H_2	99.99%	Linde
Helium	He	>99.99%	Linde
Argon	Ar	>99.99%	Linde
Nitrogen	N_2	>99.99%	Linde
Air Zero	O_2	>99.99%	BIG (Bangkok Industrial Gas)

3.2 Photocatalytic CO_2 reduction measurement

The photocatalytic CO_2 reduction was operated in the slurry batch system, as shown in Figure 8. A sand sparger is installed in the 250 ml three-way cylindrical quartz reactor for bubbling gas to the solution. Catalyst 0.3 g was suspended into a stirred batch reactor, which contained 100 ml of DI water that control pH at 4-7 by used NaH_2PO_4, HCl 1M, and NaOH 1M as a buffer, the reactor is sealed with a rubber septum and bubbled CO_2 gas by flowing gas pass sand sparger for 30 minutes. After CO_2 saturated in DI water, the solution in the reactor was measured pH and added some buffer to control pH at the intended condition. The photocatalytic reaction started after turning on UV-light (Philips' Germicidal Ozone UV Quartz Glass UVC Bulb: 16 watts, 6 bulbs), and irradiation continued for 4 hours. The resultant gas samples were taken every 0.5 hours by using 2.5 ml gas-syringe and analyzed by using GC-FID and GC-TCD, Liquid sample was taken only 1 sample at the end time of reaction for analysis with NMR.
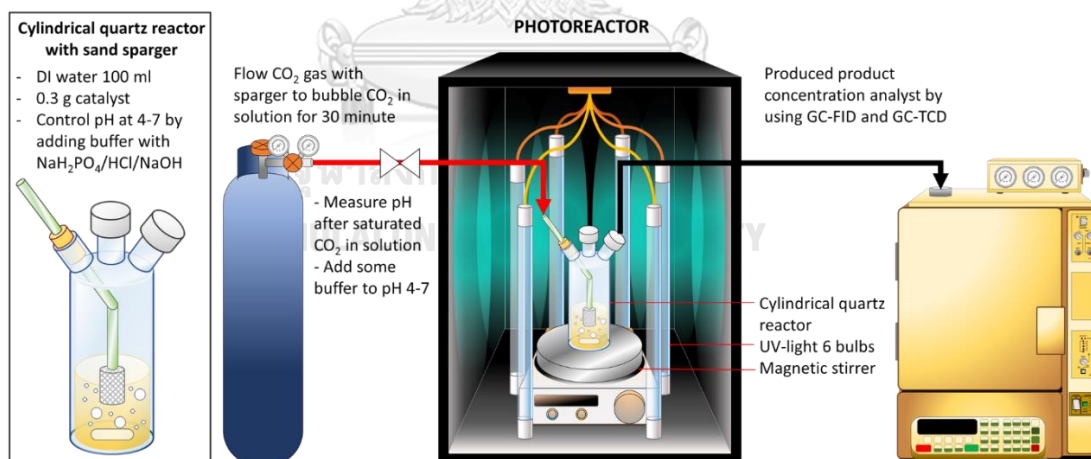
Figure 8 Schematic representation of the photocatalytic CO_2 reaction system.

3.3 Photocatalytic HCO_3^- reduction measurement

The HCO_3^- photocatalytic reduction was operated in the slurry batch system, as shown in Figure 9. The cylindrical quartz reactor with 250 ml of total volume. UV-light bulbs (Philips' Germicidal Ozone UV Quartz Glass UVC Bulb: 16 watts, 6 bulbs) were installed around a cylindrical quartz reactor. Catalyst 0.3 g was suspended into a stirred batch reactor by magnetic stirred, which contained 100-600 mg dissolved $NaHCO_3$ in 100 ml of DI water that control pH at 4-7 by used NaH_2PO4, HCl 1M, and NaOH 1M as a buffer. Then high purity of Argon gases was purged into the reactor for 5 minutes by flowing gas pass the long needle to eliminate air out from reactor at ambient pressure. After that, the reactor was closed during the reaction with a rubber septum. The photocatalytic reaction was started by turning on UV-light, and irradiation was continued for 4 hours. The resultant gas samples were taken every 0.5 hours by using 2.5 ml gas-syringe and analyzed by using GC-FID and GC-TCD, Liquid sample was taken only 1 sample at the end time of reaction for analysis with NMR.
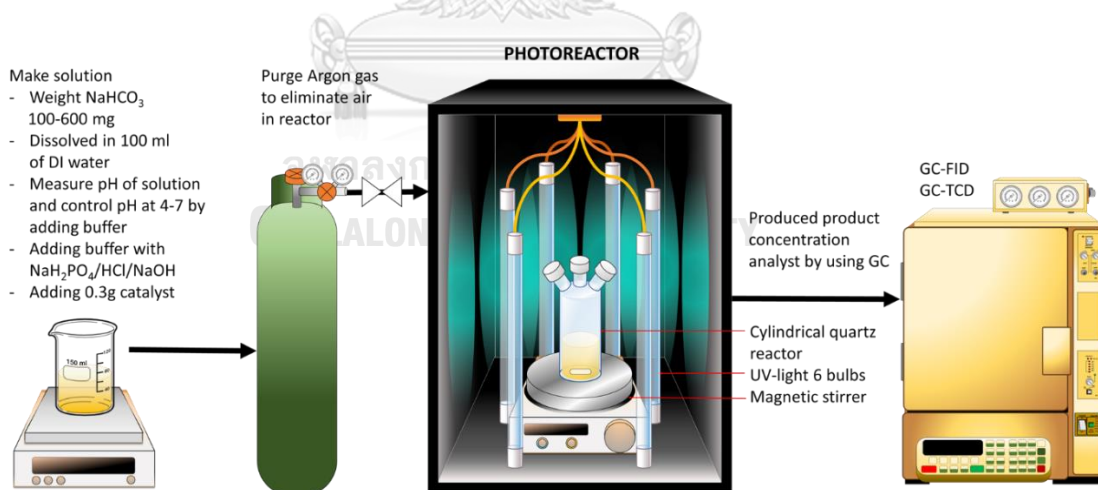
Figure 9 Schematic representation of the photocatalytic HCO_3^- reaction system.

3.4 Langmuir–Hinshelwood mechanism

Langmuir-Hinshelwood (LH) kinetic rate (r) expression is shown in Eq. 37.

$$r = -\frac{d[C]}{dt} = \frac{kK[C]}{1+K[C]}$$
Eq. 37

If CO_2 or HCO_3^- as substrate at initial of process, LH model is expressed as shown in Eq.38 and 39

CO_2 photoreduction: $r_i = -\frac{d[CO_2]_i}{dt} = \frac{kK[CO_2]_i}{1+K[CO_2]_i}$
Eq. 38

HCO_3^- photoreduction: $r_i = -\frac{d[HCO_3^-]_i}{dt} = \frac{kK[HCO_3^-]_i}{1+K[HCO_3^-]_i}$
Eq. 39

Where r_i represent the initial rate of reaction

            [ ]$_i$ represent the initial concentration of substrate

            k represents the rate constant at maximum adsorption.

            K represents adsorption on catalyst constant

And $k_{obs} = kK$
Eq. 40

The initial rate of reaction (r_i) in each condition of the experiment can be achieved from the linearity relation of produced hydrocarbon concentration with the reaction time. The constant values (k, K) can be obtained from the relation of the initial rate of reaction by calculating the slope on the graph before.

3.5 H_2O/D_2O Isotope effect of photocatalytic HCO_3^- reduction on P25 as photocatalyst

The H_2O/D_2O Isotope effect in photocatalytic HCO_3^- reduction was operated in the same batch system, as shown in Figure 9. The cylindrical quartz reactor with 250 ml of total volume. 0.03 g of P25 as photocatalyst were suspended into a stirred batch reactor containing 60 mg of dissolved $NaHCO_3$ in 10 ml of DI water. pH at 7 was maintained using NaH_2PO_4, HCl 1M and NaOH 1M as a buffer. Then high purity of Argon gas was bubbled into the reactor for 5 minutes to purge air at ambient pressure. After that, the reactor was closed with septum during the reaction. The photocatalytic

reaction was started by turning on UV-light, and irradiation was continued for 3 hours. The resultant gas samples were taken every 0.5 hours by using 2.5 ml gas-syringe and analyzed by using GC-FID and GC-TCD.

3.6 Sonicated P25 photocatalyst preparation

Sonicated P25 was prepared by dispersing 10 g of Degussa P25 powder (TiO_2 consist of 75% anatase and 25% rutile phases) in 150 ml water. Sonicated for 30 minutes, centrifuged to separate the water and dried in the oven at 110 °C overnight.

3.7 Reaction analysis equipment

3.6.1 Gas-Chromatography

Table 4 Condition of Gas-Chromatography

Gas chromatography	Shimadzu GC-14A	Shimadzu GC-8A
Detector	FID	TCD
Packed column	Shincarbon ST	Molecular sieve 5A
Carrier gas	He (HP grade, 99.99 vol.%)	Argon (HP grade, 99.99 vol.%)
Make-up gas	Air (UHP grade, 100 vol.%)	-
Column temperature	70 °C	70 °C
Injector temperature	150 °C	150 °C
Detector temperature	150 °C	150 °C
Time analysis	10 minutes	18 minutes
Analyzed product	CH_4	H_2, CO

Conversion and Selectivity calculation

Conversion of this photocatalytic reduction is determined by using the concentration of product at the end time of reaction, initial concentration of substrate as the following equation.

$$\text{Conversion (\%)} = [HCP]_{t(end)} \times 100\% / [C]_0 \qquad \text{Eq. 41}$$

Where $[HCP]_{t(end)}$ is Hydrocarbon concentration at the end time of reaction.

$[C]_0$ is the initial concentration of the substrate.

The selectivity of this photocatalytic reduction is considered from the concerned product concentration.

$$\text{Selectivity (\%)} = [P]_{t,i} \times 100\% / [HCP]_t \qquad \text{Eq. 42}$$

Where $[HCP]_t$ is Hydrocarbon concentration at the time of reaction.

$[P]_{t,i}$ is the Concentration of concern product at the time of reaction.

3.6.2 Nuclear magnetic resonance spectrometer (NMR)

Nuclear magnetic resonance spectrometer (NMR) was used for analyzing organic compounds produced at the reactor liquid phase by measuring the FID signal that generated the nuclear emission energy. This energy occurs from the excited element nucleus by using radiofrequency waves.

For produced product in liquid phase such as Methanol (CH_3OH), Formic acid ($HCOOH$) in a large amount of water is analyzed by using Fourier Transform Nuclear Magnetic Resonance Spectrometer 500 MHz (NMR 500 MHz) that perform by BRUKER AVANCE III HD/OXFORD 500 MHz with Solvent peak suppression program.

The NMR sample is prepared by using 400 μL of the liquid sample from reaction with 200 μL internal standard that content with 0.012 μmol/mL of phenol and 0.125 μL/mL of DMSO (Dimethyl sulfoxide) in D_2O (Deuterium oxide).

The product compound and phenol peak position were specified by comparing with the DMSO peak position, then compare the product peak area with phenol peak area to calculate the concentration of product in the NMR sample.

The calculation of liquid product in the sample as follows:

Phenol: Phenol has 5 atoms of aromatic Hydrogen in the molecule

Phenol area integration from NMR = (Phenol NMR area)

Phenol concentration in NMR sample = [Phenol] or [C_6H_5OH]

Methanol: Methanol has 3 atoms of Hydrogen bind carbon in the molecule

Methanol area integration from NMR = (Methanol NMR area)

Methanol concentration in NMR sample = [Methanol] or [CH_3OH]

Therefore, Methanol concentration in the NMR sample is

$$[\text{Methanol}] = \frac{[\text{Phenol}] \times \frac{3}{5} \times (\text{Methanol NMR area})}{(\text{Phenol NMR area})} \qquad \text{Eq. 43}$$

3.8 Characterization equipment

3.8.1 X-ray diffraction (XRD)

The phase crystal structure of the compound was analyzed by the X-ray diffraction technique (XRD) that used X-ray diffractometer (Bruker D8 Advance) with Cu anode, K_{α}1-1,544 A° irradiation at various angles between 20 deg and 80 deg with a resolution of $0.05°s^{-1}$. Specify the phase crystal structure type by comparison and confirmation from JCODS database: JCPDS card no.21-1272 (anatase TiO_2), JCPDS card no.21-1276 (rutile TiO_2). The Debye-Scherrer equation calculated the crystallite size.

3.8.2 X-ray photoelectron spectroscopy (XPS)

The binding energy and surface composition (oxidation state) were investigated by X-ray photoelectron spectroscopy (XPS). XPS used an AMICUS photoelectron spectrometer with Mg K_{α} X-ray source is controlled by KRATOS VISION2 software at a current of 20 mA and 10 KeV. Furthermore, the intensity of Ti 2p and O 1s were intense at binding energy 455-470 eV and 525-540 eV respectively after that the oxidation state species of each element were indicated from NIST XPS database.

3.8.3 UV-VIS Spectroscopy (UV-VIS)

The UV-visible absorption spectra of catalyst molecules were detected by Spectroscopy using LAMDA 650 UV/Vis spectrophotometer with wavelength varying between 100-900 nm in the ultraviolet and visible light wavelength (UV-C wavelength is 100-280 nm and 380-740 nm). The light absorption data were obtained by UV Win Lab software from PerkinElmer. UV-VIS result shows diffuse reflectance spectra of catalysts, and the energy band gap can be calculated from its optical absorption edge with Tauc's equation Eq. 34.

$$\alpha h\nu = A(h\nu - E_g)^m \qquad\qquad\qquad \text{Eq. 43}$$

where A is the optical constant, h is Planck's constant, α is the absorption coefficient, ν is c/λ that c is the speed of light in vacuum and λ is the wavelength, E_g is the optical band gap, and m value is 0.5 for direct transitions and 2 for indirect transitions.

3.8.4 Photoluminescence spectroscopy (PL)

The charge separation and the charge-carrier lifetime of catalyst were investigated by Horiba 4P-Fluoromax spectrofluorometer. Photoluminescence spectroscopy used Xenon lamp as the excitation source. Excitation was investigated under wavelength 200-800 nm. The light beam was used to excited the electron in molecule become to an excited state (minority carrier) after that, the excited electron goes down to the equilibrium state. The process of minority carrier recombination a small period of time is known as charge-carrier lifetime.

3.8.5 N_2-Physisorption

N_2 adsorption–desorption experiments were performed to the catalysts at -196 °C by under vacuum 12 hours the multipoint Brunauer–Emmett–Teller (BET) method on a Micromeritics ASAP 2020 instrument. Before the measurement, each sample was degassed under vacuum at 150 °C for 8 h.

CHAPTER IV
RESULTS AND DISCUSSION

In this chapter, the physiochemical properties and the catalytic performance of the catalyst were discussed. In this work, the photocatalysts are the pure commercial titanium dioxide (P25) and the sonicated titanium dioxide (Sonic.P25). Both P25 and Sonic.P25 catalysts were characterized by using several techniques as XRD, XPS, N_2 physisorption, UV-vis, PL and SEM. The photocatalytic performance for the conversion and selectivity of CO_2 and HCO_3^- photoreduction to hydrocarbon products, changing P25 morphology, alternative CO pathway formation and H_2O/D_2O solvent isotope effect is reported.

4.1 Characterization

4.1.1 Powder X-ray diffraction (XRD)

The X-ray diffraction pattern of commercial TiO_2 (P25) and Pre-treatment TiO_2 (Sonic.P25) catalyst were shown in Figure 10. Both catalysts consist of two mixture phases, containing the anatase phase and the rutile phase with the same characteristic peaks. The anatase phase of catalysts has 2threta (2θ) and Miller indices is 25.3° (101) main peak, 37.0° (103), 37.8° (004), 38.5° (004), 48° (200), 54.3° (105), 55.1° (211), 62.8° (213), 70.3° (220) and 75.1° (215). The rutile phase is 27.4° (110) main peak, 36.1° (101), 41.3° (111), 53.9° (221), 56.6° (220) and 69.0° (301) [61-63]. The phase composition of catalyst is calculated from the integrated intensities of anatase and rutile phases. The weight fraction of anatase and rutile phases which consist of 80% anatase and 20% rutile phases in both catalysts.

The average crystallite size of anatase and rutile phases was calculated from the main anatase and rutile peak (2threta = 25.3° and 36.1°) using the Debye-Scherrer equation [64]. The crystallite size of anatase and rutile phases in P25 is 18.68 nm and

29.24 nm. The Sonic.P25 crystallite size of anatase and rutile phases are slightly smaller than P25 with 18.33 nm and 28.29 nm, respectively. In consequence, the ultrasonic vibration of sonicate pre-treatment can slightly reduce the size of the crystal and does not change the crystal phase structure of the catalyst.
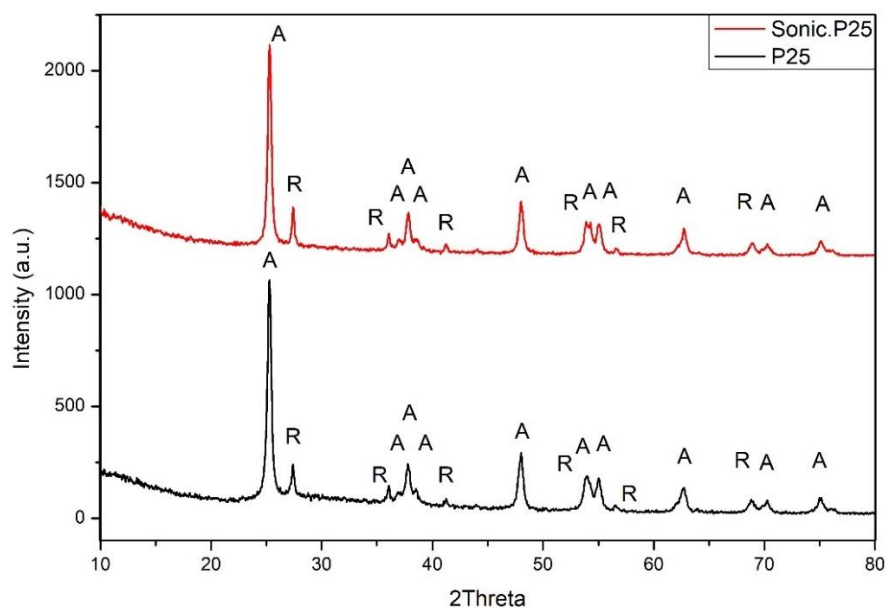
Figure 10 XRD pattern of P25 and Sonic.P25 catalyst.

4.1.2 X-ray photoelectron spectrometer (XPS)

The XPS binding energy of element composite in the catalyst is shown in Figure. 11-12. The O1s peak of O_L at 529.8 eV is oxygen lattice of oxygen bonding with Ti^{4+} in Ti-O-Ti. O_V at 531.5 eV is Oxygen vacancy or non-oxygen lattice that is OH group with oxygen binding site on the catalyst surface and O_S at 533.4 eV may be chemisorbed oxygen specie on the catalyst surface that is oxygen attached to another impurity element [65-67]. The binding energy of Titanium (Ti2p), Ti(2p2) at 458.6 eV is Ti^{4+} and Ti(2p1) at 456.8 eV is Ti^{3+} in TiO_2. The Ti^{3+} indicates oxygen vacancies. The Ti^{3+} was generated to maintain electrostatic balance according to Ti^{4+} and O^{2-} to the vacant position of oxygens in TiO_2 [68]. Including to the peak area, Ti^{3+}/Ti^{4+} and O_V/O_L area ratios are 0.017 and 0.43 for P25 and 0.022 and 0.79 for Sonicated P25, respectively.

From Table 5, the sonicated P25 has more oxygen vacancy on its surface that could promote more photoactivity of catalyst.
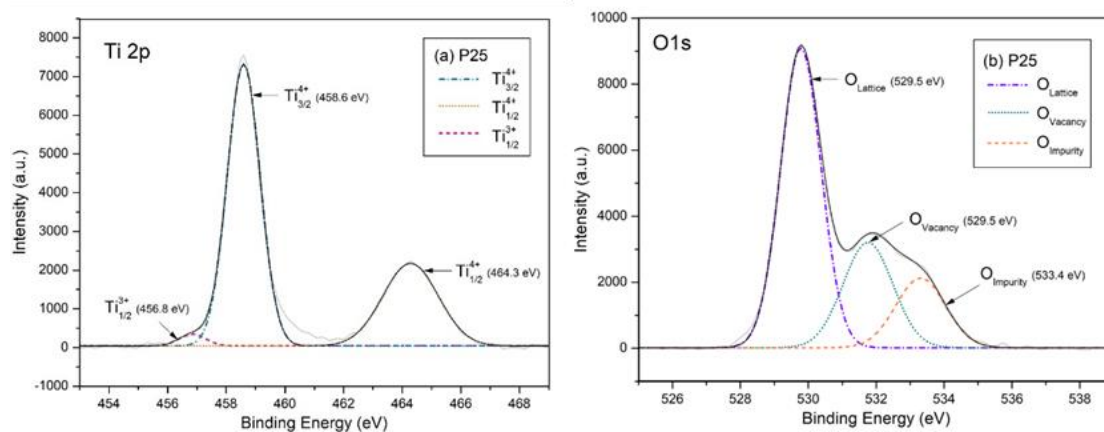

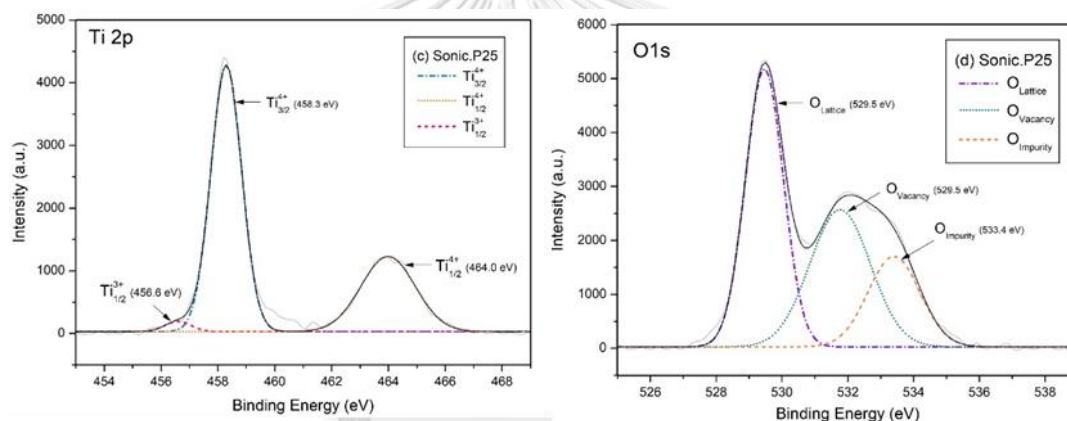**Figure 11** XPS spectra of (a).Ti 2p and (b). O1s of P25 catalyst

Figure 12 XPS spectra of (a).Ti 2p and (b). O1s of Sonic.P25 catalyst

Table 5 The ratios of Ti^{3+} to Ti^{4+} and O_V to O_L of catalysts.

Catalyst	Ratio Ti2p (Ti^{3+}/Ti^{4+})	Ratio O1s (O_V/O_L)
P25	0.017	0.432
Sonic.P25	0.022	0.787

4.1.3 Surface Area Measurement

The surface area of P25 and Sonic.P25 catalyst are specified by using the single-point N_2 physisorption analysis. The P25 and Sonic.P25 have a surface area of 51.34 m^2/g_{cat} and 51.48 m^2/g_{cat}, respectively. Therefore, the sonication was not effect to surface changing in TiO_2 catalyst.

4.1.4 UV-vis absorption spectra

The UV-vis absorption spectra are used to investigate the light absorption of P25 and Sonic.P25, as shown in Figure 13. The sharp absorption band at wavelengths less than 400 nm were associated with the band structure of the catalysts, which is the light region that can excite an electron to transfers from the valence band to the conduction band. The absorption edge of P25 was located at 373 nm, which the catalyst adsorbs the UV-light only while the Sonic.P25 can slightly adsorb the visible light (wavelength > 400 nm) because the absorption edge was located at 404 nm.
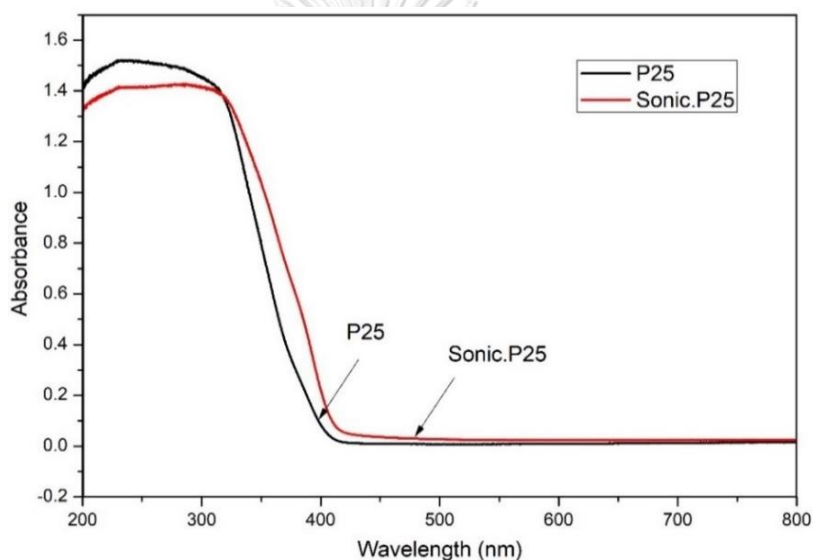
Figure 13 UV-vis absorbance spectra of P25 and Sonic.P25.

From the light absorbance of catalyst at each wavelength, as shown in Figure 13, the energy band gap of P25 and Sonic.P25 catalyst were inferred by using the Tauc's relation (Eq.43) as shown in Figure 14. The plot of $(\alpha h\nu)^2$ versus the photoenergy ($h\nu$) of each catalyst shown the curve line, which intercepted on the photoenergy as its bandgap energy [69]. The P25 had the wider energy bandgap about 3.22 eV, compared to the Sonic.P25 that had the energy bandgap about 2.97 eV. The narrower energy bandgap of Sonic.P25 resulted in the electrons transferred from the valence band to the conduction band more efficiently [70, 71].
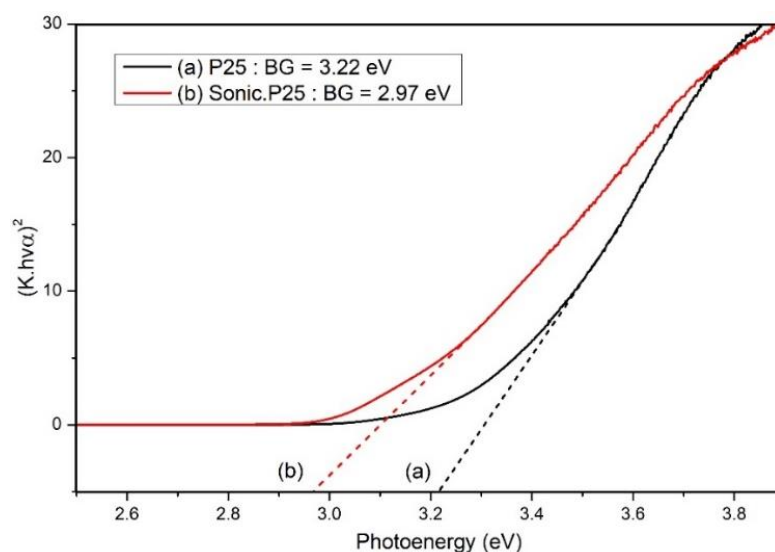
Figure 14 Tauc's relation for energy band gap determination of P25 and Sonic.P25

4.1.5 Photoluminescence (PL)

The photoluminescence (PL) is a technique for measuring the efficiency and electrical properties of semiconductors such as charge carrier trapping, carrier lifetime and recombination [72]. The results from the light radiation or photon energy emission from the catalyst sample after absorbed the laser-light energy, as shown in Figure 15. Generally, the semiconductor has an electrical property called the energy bandgap, which is the gap of energy level between the conduction band and valence band. When the electrons in the valence band adsorb the light energy more than the energy band gap, then the electrons are excited to the conduction band. But if the adsorbed light energy is not stable or not enough, the excited electrons will go back to the valence band and emit the photon energy [73]. The photo energy emission of electrons in going back to the valence band is the recombination of e^-/h^+ pair. The PL emission spectra of catalysts is shown in Figure 15. The intensity indicates the emission energy of e^-/h^+ recombination rate. P25 had intensity of emission energy more than Sonic.P25. Therefore, the sonicated treatment contributes more charge separation and reduces the recombination rate in the catalyst.

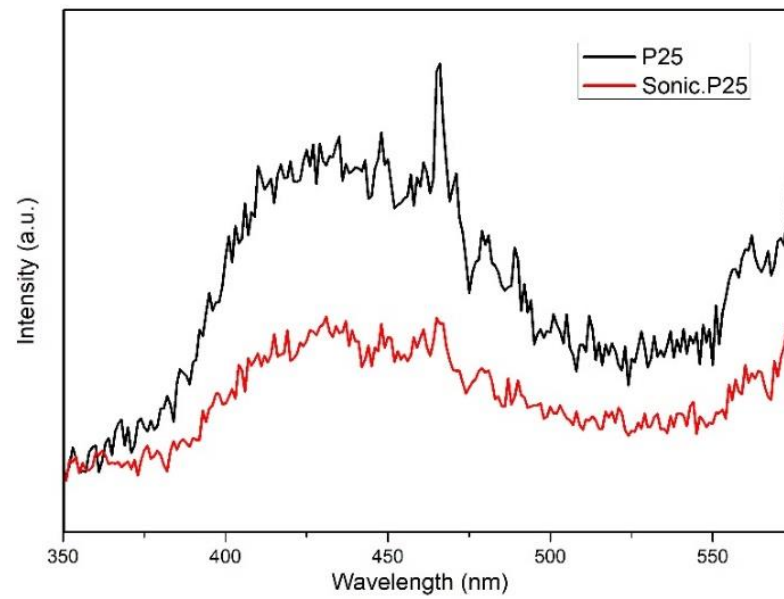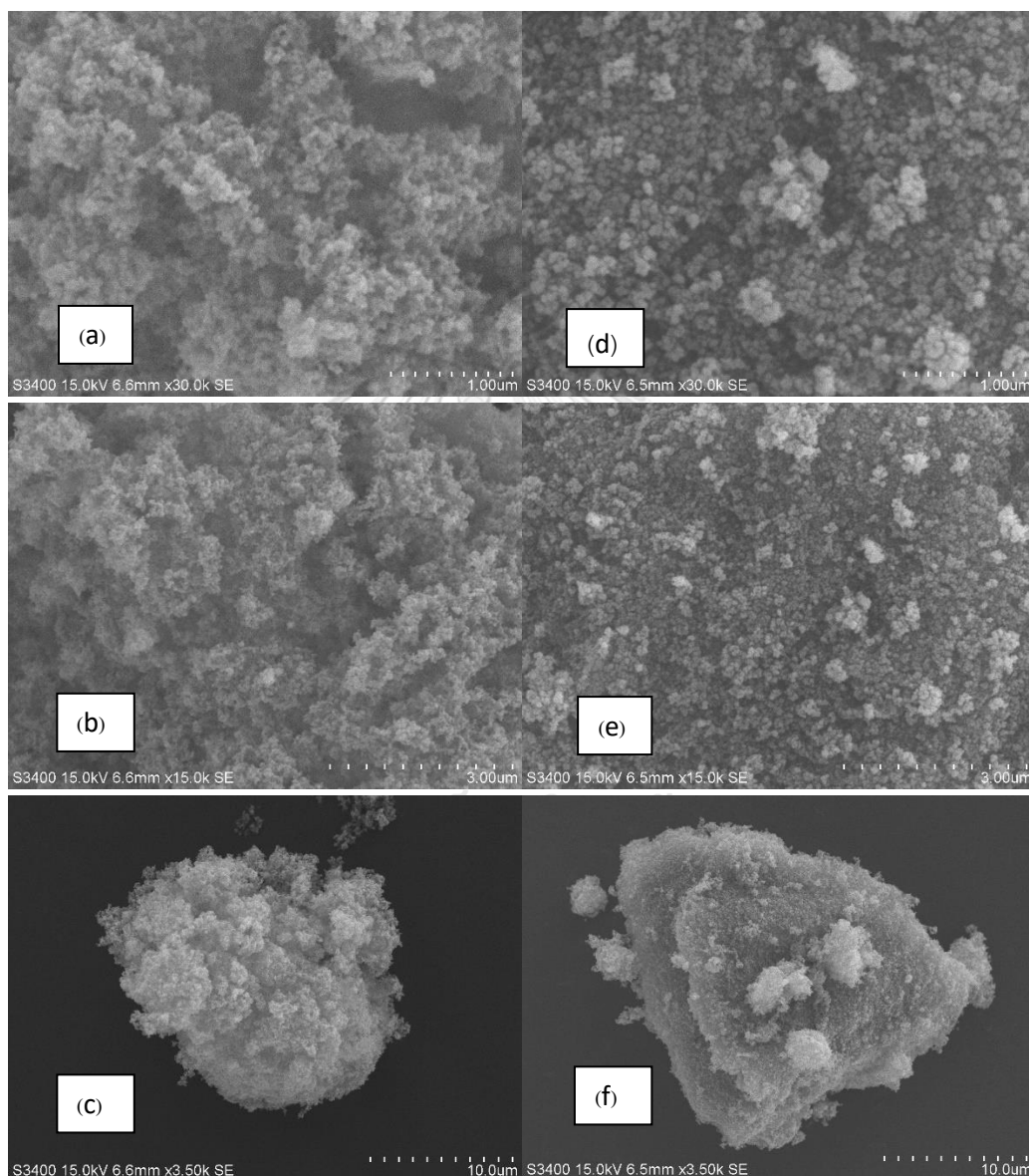**Figure 15** The PL emission spectra of P25 and Sonic.P25

4.1.5 Scanning electron microscopy (SEM)

The morphology of P25 and Sonic.P25 particle, are presented in Figure 16; these micrographs can not be explained by the anatase and rutile phase mixing. The spherical nanoparticles of P25 and Sonic.P25 is not much different from the sonication.

Figure 16 SEM images of (a-c) P25 and (d-f) Sonic.P25 catalyst

4.2 CO$_2$ Photoreduction experiments

From CO$_2$ photoreduction experiment, the P25 catalyst was used under the initial concentration of CO$_2$ in water is $[CO_2]_{w0}$ = 34 x 10^3 nmol/ml$_{H2O}$ at pH = 5.41, 5.12 and 4.52, Temperature 45 °C. The detected products in the headspace of the reactor are CH$_4$, CO and H$_2$. As shown in Figure 17(a), the initial production rate of CH$_4$ is 1.4-1.6 nmol/ml$_{H2O}$.g$_{cat}$.h, 3.2-3.9 nmol/ml$_{H2O}$.g$_{cat}$.h for CO, 8.3-11.8 nmol/ml$_{H2O}$.g$_{cat}$.h for H$_2$. The selectivity is 9%, 20%, 71% for CH$_4$, CO and H$_2$, respectively. Selectivity slightly changes when changed to other pH values, as well as the production rate of CO and H$_2$ obtained from the plot of product concentration versus time in Figure 17 (c-d). Furthermore, in the aqueous phase was found a minimal amount of methanol compared to other products, CH$_3$OH initial production rate = 0.10 nmol/ml$_{H2O}$.g$_{cat}$.h at pH 4.52 measured by HNMR. From Table 6, conversion of each product is very low (%conversion of approximately 6.3 x 10^3%, 14.1 x 10^3 % and 36.6 x 10^3 % for CH$_4$, H$_2$, and CO production).

Table 6 CH$_4$, H$_2$ and CO conversion and selectivity from CO$_2$ photoreduction in the aqueous phase under P25 catalyst performance at pH = 5.42, 5.12 and 5.42, Temperature 45 °C.

pH	% Conversion x 10^3 [*a]			% Selectivity [*b]		
	CH$_4$	H$_2$	CO	CH$_4$	H$_2$	CO
5.4	6.3	14.1	36.6	9.7	22.7	67.6
5.1	6.7	15.0	39.4	10.8	23.8	65.5
4.5	7.0	17.0	51.9	8.8	20.4	70.8

*a. Calculated using: %Conversion = $r_i/[CO_2]_{iw}$,

where $[CO_2]_{w0}$ = 1 atm/29.41 atm/M = 34 μmole/ml = 34 x 10^3 nmole/ml.

*b Calculated from products detected at the headspace in reactor : CH$_4$, CO and H$_2$.
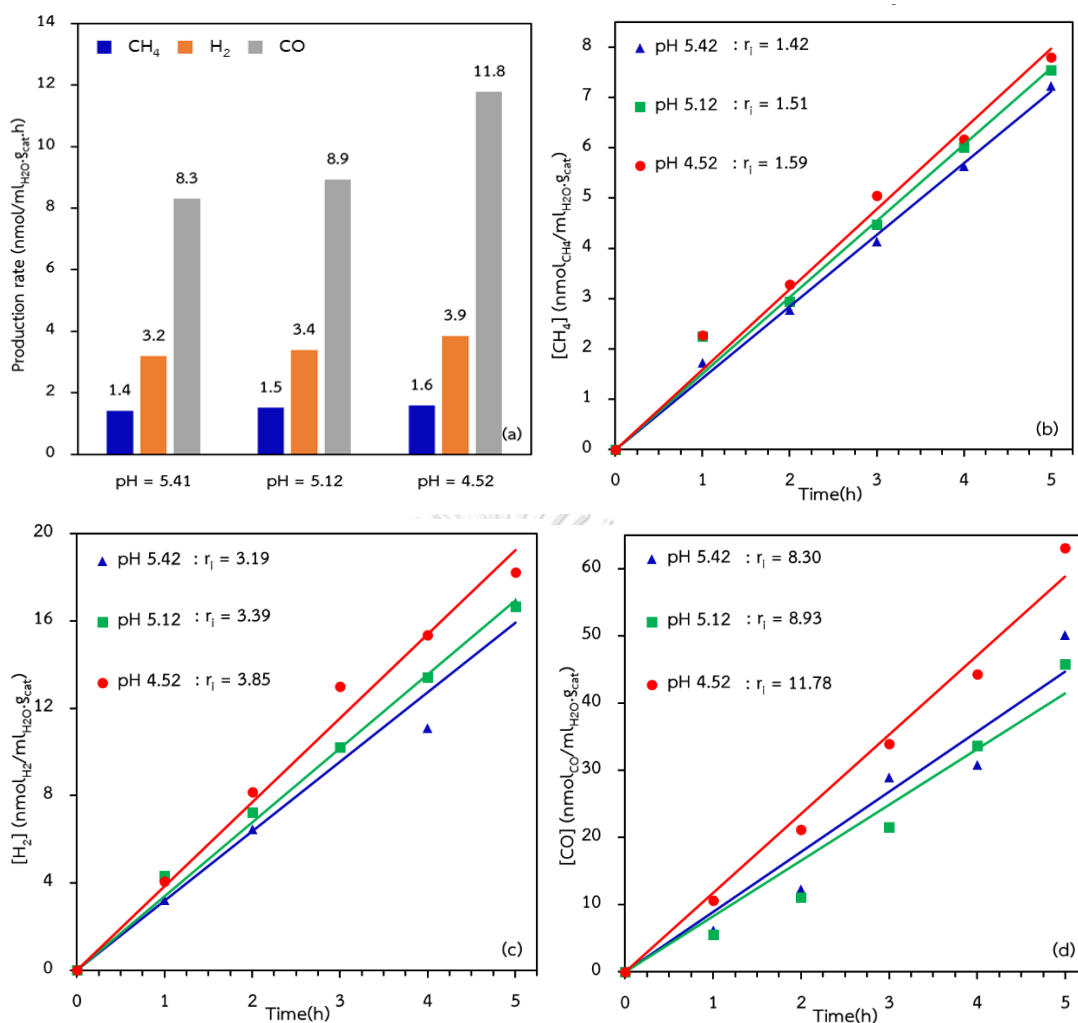
Figure 17 CO_2 photoreduction result under P25 catalyst performance (a). Rates of
CH_4, H_2 and CO production at pH = 5.42, 5.12 and 5.42.
(b-d). Initial rates of CH_4, H_2 and CO production at pHs studied.
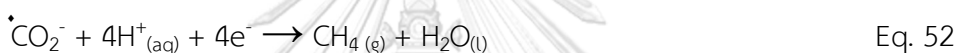
The CH_4 formation pathways of CO_2 photocatalytic on TiO_2 with H_2O have been proposed [73]. These pathways involved homolytic bond cleavage and formation (Eq. 46-48). Firstly, the adsorbed CO_2 is reduced to form the radical anion $^•CO_2^-$ at the conduction band (Eq. 44), while water is oxidized at the valence band to form $^•OH$ and $^•H$ radicals (Eq. 45). The radical anion $^•CO_2^-$ continuous reducing to form $^•CO$ (Eq. 46). Then $^•CO$ and $^•H$ radicals will bond to form C-H radicals to form CH_4 (Eq. 47-48) [74]. For the H_2, CO, CH_4 and CH_3OH heterolytic formation pathway, These product

formation pathways, consisting of $\overset{\bullet}{C}O_2^-$ and H^+ binding has been proposed as shown in Table 2 or Eq. 50-52 [75].

$$CO_2 + e^-_{CB} \longrightarrow \overset{\bullet}{C}O_2^- \qquad \qquad \text{Eq. 44}$$

$$H_2O + h^+_{VB} \longrightarrow \overset{\bullet}{H} + \overset{\bullet}{O}H \qquad \qquad \text{Eq. 45}$$

$$2\overset{\bullet}{C}O_2^- + 2e^-_{CB} \longrightarrow 2\overset{\bullet}{C}O + O_2 \qquad \qquad \text{Eq. 46}$$

$$2\overset{\bullet}{C}O + 4\overset{\bullet}{H} \longrightarrow 2\overset{\bullet}{C}H_2 + O_2 \qquad \qquad \text{Eq. 47}$$

$$2\overset{\bullet}{C}H_2 + 2\overset{\bullet}{H} \longrightarrow 2CH_4 \qquad \qquad \text{Eq. 48}$$

$$2H^+ + e^- \longrightarrow H_2 \qquad \qquad \text{Eq. 49}$$

$$\overset{\bullet}{C}O_2^- + 2H^+_{(aq)} + 2e^- \longrightarrow CO_{(g)} + H_2O_{(l)} \qquad \qquad \text{Eq. 50}$$

$$\overset{\bullet}{C}O_2^- + 6H^+_{(aq)} + 6e^- \longrightarrow CH_3OH_{(aq)} + H_2O_{(l)} \qquad \qquad \text{Eq. 51}$$

$$\overset{\bullet}{C}O_2^- + 4H^+_{(aq)} + 4e^- \longrightarrow CH_{4\,(g)} + H_2O_{(l)} \qquad \qquad \text{Eq. 52}$$
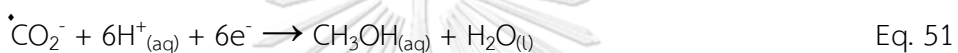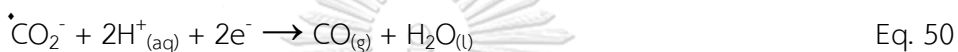
If the rate limiting step in CO_2 photoreduction is the radical anion formation $\overset{\bullet}{C}O_2^-$ (Eq. 44), the homolytic or heterolytic paths occur after this step; therefore, they cannot be distinguished kinetically. The intermediate formation of $\overset{\bullet}{C}O_2^-$ is the rate limiting step for CO_2 photocatalytic reduction [76], but the product yields depend on the reaction condition or the used solvent that promote faster pathways. In experiments, the water is the polar media that favoured for heterolytic intermediate formation pathway as Eq. 50-52. These product formations must follow the reduction potential of reaction. The CO_2 photoreduction potential to CO, CH_3OH, CH_4 and H_2 are -0.52, -0.38, -0.34 and 0, respectively [77]. According to these values, the products partitioning order must be $H_2 > CH_4 > CH_3OH > CO$.

However, CO has a different order of product formation at all pH, as shown in Figure 17. In fact, $[CO]/[CH_4]$ increases with time, as shown in Figure 18(a): therefore, additional CO formation is obtained with time meaning that there're is another pathway that contributes with additional CO formation. If there is only one CO pathway contribution, $[CO]/[CH_4]$ ratio should be maintained constant with time. There is also

an initial increase of the $[H_2]/[CH_4]$ ratio that was increased in the initial period and turn bank to t_0 ratio (Figure 18(b)). The alternative pathway formation for CO and H_2 production reaches a maximum contribution at 3 h. After that time, ratios return to the initial ratio at t_0 (Figure 18(a, b)). The t_0 contributions are given by estimating the intersection straight lines to t = 0. These ratio values are 1.8, 3.1 and 4.3 at pH = 5.12, 5.41 and 4.51, respectively for $[CO]/[CH_4]$ and 1.7 for $[H_2]/[CH_4]$. This means that CH_4 selectivity ($[CO]/[CH_4]$ at t_0) increases at lower pH. From the maximum ratio in Figure 18, the alternative pathway contribution can also be estimated. From these maximum values, it can be concluded that CO is produced twice as a large amount as H_2.
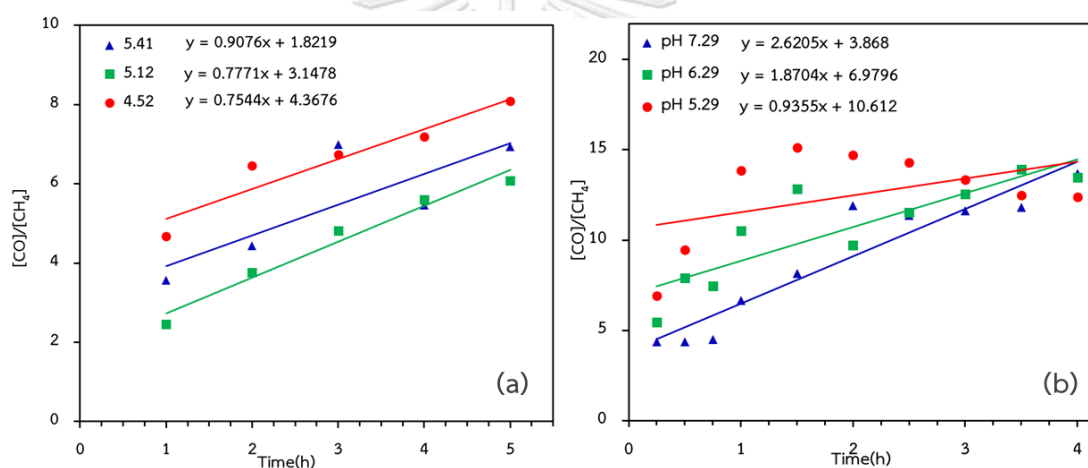
Figure 18 CO_2 Photoreduction products ratios of (a). $[CO]/[CH_4]$ and (b). $[H_2]/[CH_4]$ Vs. reaction time by P25 performing at different pH.

According to Figure 19, the proposed photoreduction mechanism in the gas phase is limited by the $\overset{\bullet}{C}O_2^-$ radical anion formation formed via previous equilibrium of direct addition of reactant molecule to TiO_2. However, in the aqueous phase is limited by carbene formation ($R\text{-}\overset{\bullet\bullet}{C}\text{-}R$) via previous equilibrium [1]. The radical anion and the carbene pathway finally form CO, H_2, CH_4 and CH_3OH. According to the $[CO]/[CH_4]$ and $[H_2]/[CH_4]$ ratios at t = 0, partitioning to CO is favored in a ratio 2-4. However, a contribution from the oxygen vacancies sites (O_V) also occurs at early reaction times

(Figure 20) to produce 2 moles of CO and 1 mole of H_2 [78] by adding oxygen from reactant to V_0, as experimental ratios of Figure 18. From Figure 19, the partitioning 3 produces formate radical anion that has been detected by EPR [79]. It is formed via homolytic rupture of the O-C bond and heterolytic cleavage of the O-H bond at the radical anion adduct.
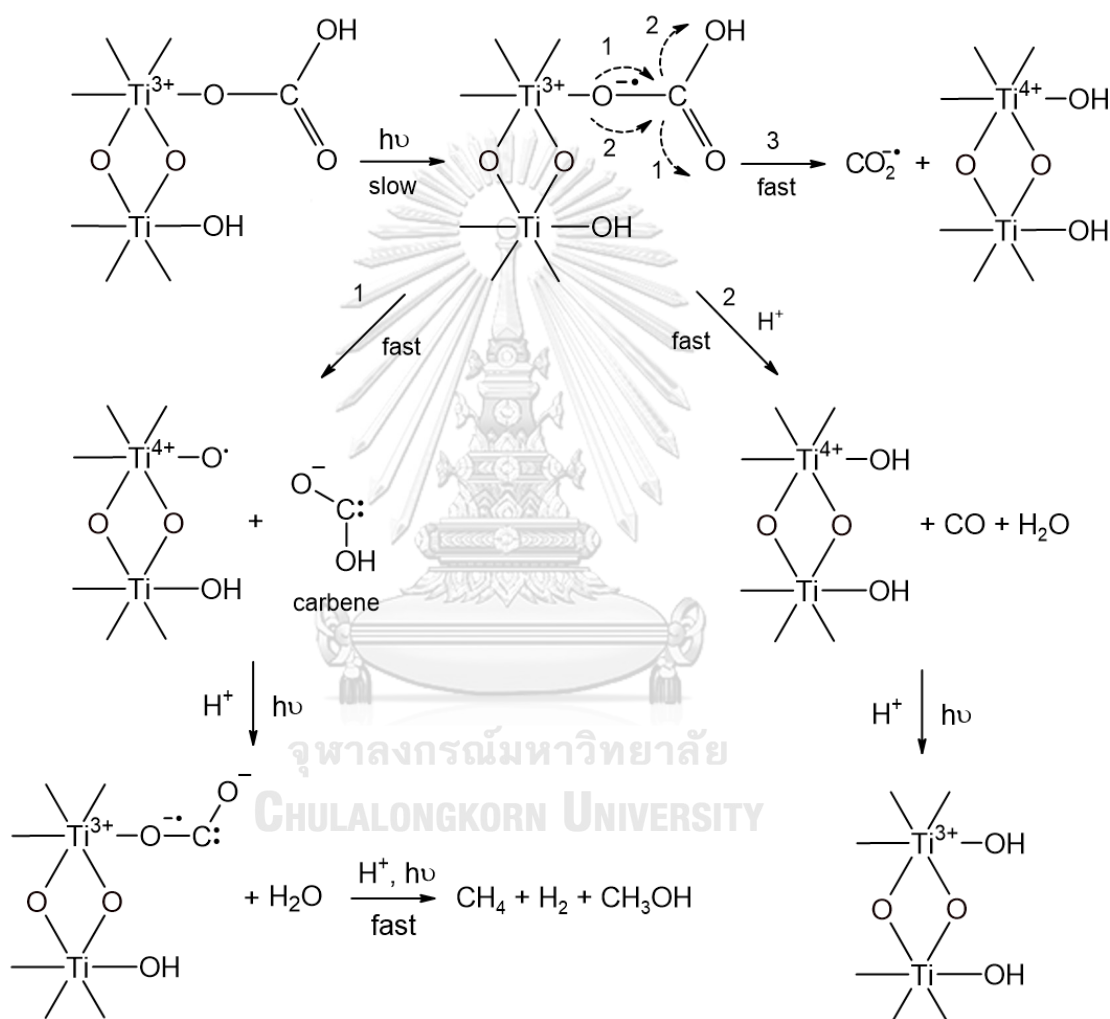
Figure 19 Reaction mechanism and kinetic (t_0) path for CO, H_2, CH_4 and CH_3OH formation. Partitioning 2 is acid catalyzed. [CO]/[CH_4] increases when decreasing pH. Formate radical anion $^\bullet CO_2^-$ (partitioning 3) has been detected by EPR [79]
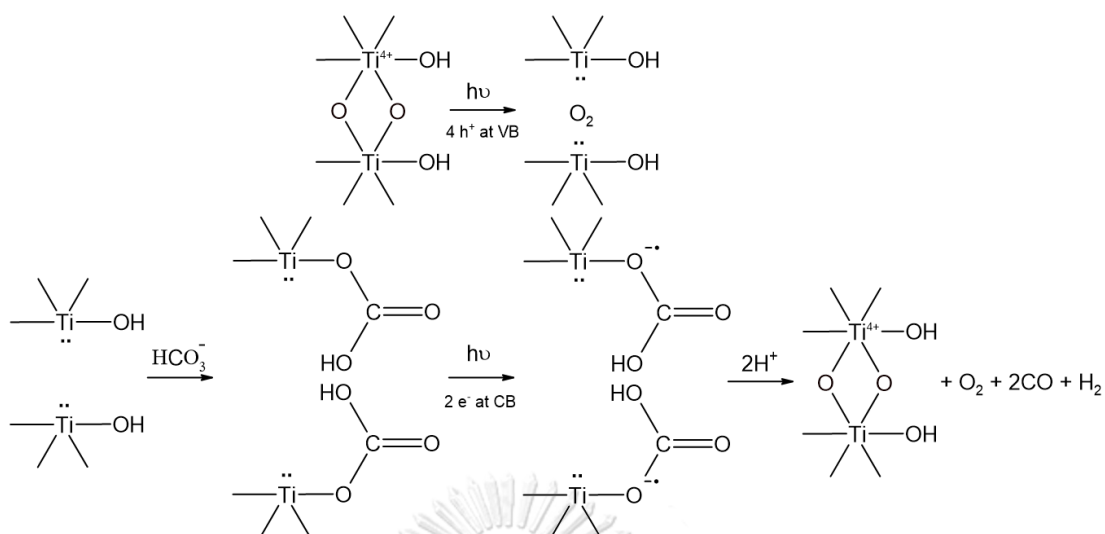
Figure 20 Top: Oxygen vacancies (O_V) produced by O_2 evolution promoted by light at the TiO_2 VB. Bottom: Additional path for CO and H_2 formation at the P25 oxygen vacancies. A 2:1 CO: H_2 is produced at early reaction times after t=0 until a maximum [CO]/[CH$_4$] is reached [37].

4.3 HCO_3^- photoreduction experiments

HCO_3^- Photoreduction on P25 catalyst kinetic experiments were conducted. It has been proposed that using HCO_3^- as reactant CO, CH_4 and CH_3OH (Eq. 29-30) are produced [80]. Therefore, $NaHCO_3$ solid has been used in this work in order to obtain better controlled conditions of the system studied. The sodium cation (Na^+) from $NaHCO_3$ dissolution has been reported that no effects on the photoreactions are observed [81] because Na^+ is not favored to adsorb on the TiO_2 [82]. Consequently, the HCO_3^- photocatalytic reduction was studied under different initial concentrations ($[HCO_3^-]_0$ = 11.9-71.4 x 10^3 nmol/ml) and pH conditions (pH= 5.29-7.29). Considering similar conditions, the production rate of CH_4, H_2 and CO from initial concentration $[HCO_3^-]_0$ = 23.8 x 10^3 nmol/ml at pH = 5.29 are more than about 5 times with $[CO_2]_{0w}$ = 34 x 10^3 nmol/ml at pH = 5.41. It can be concluded that using HCO_3^- the same products as when using CO_2 are formed but rates are faster.
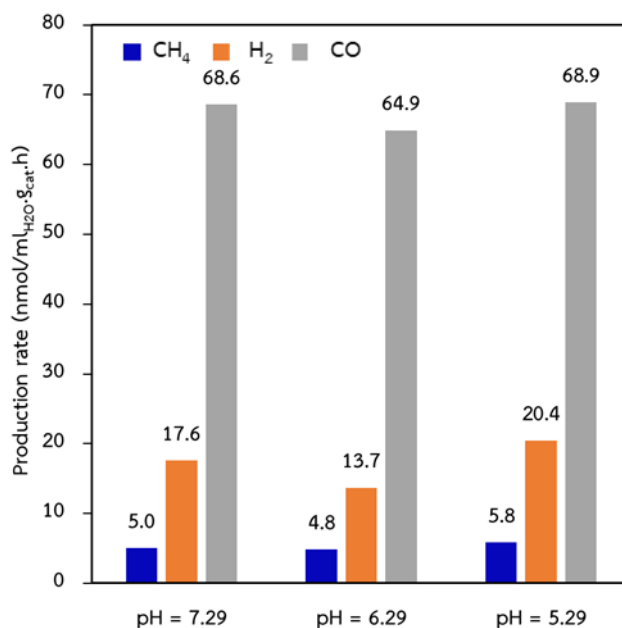
Figure 21 Production rate of HCO_3^- photoreduction on P25 under $[HCO_3^-]_0$ = 23.8 μmole/ml (23.8 x 10^3 nmol/ml), different pH, Temperature 45 °C.

Both CO_2 and HCO_3^- photoreduction must form $\overset{\bullet}{C}O_2^-$ radical anion before going to the next step (Eq. 44 and Eq. 29-30 for HCO_3^- cases). So, the rate limiting step of both cases is the formation of $\overset{\bullet}{C}O_2^-$. The different production rate must be due to the adduct formation or/and the electron transfer from Ti. As shown in Figure 22, the adduct formation on TiO_2 surface in both CO_2 and HCO_3^- photoreduction is similar. Thus, the production rate changing is not due to the electron transfer rate (k). The CO_2 hybridization is changed from sp to sp^2, when using CO_2 as the substrate[83]. On the other hand, the HCO_3^- hybridization was not changed. The different production rate between using HCO_3^- and CO_2 causes the OH on Ti was substituted to produce H_2O during adduct formation in HCO_3^- case. Consequently, the different production rate between CO_2 and HCO_3^- cases must come from the adsorption equilibrium constant (K).
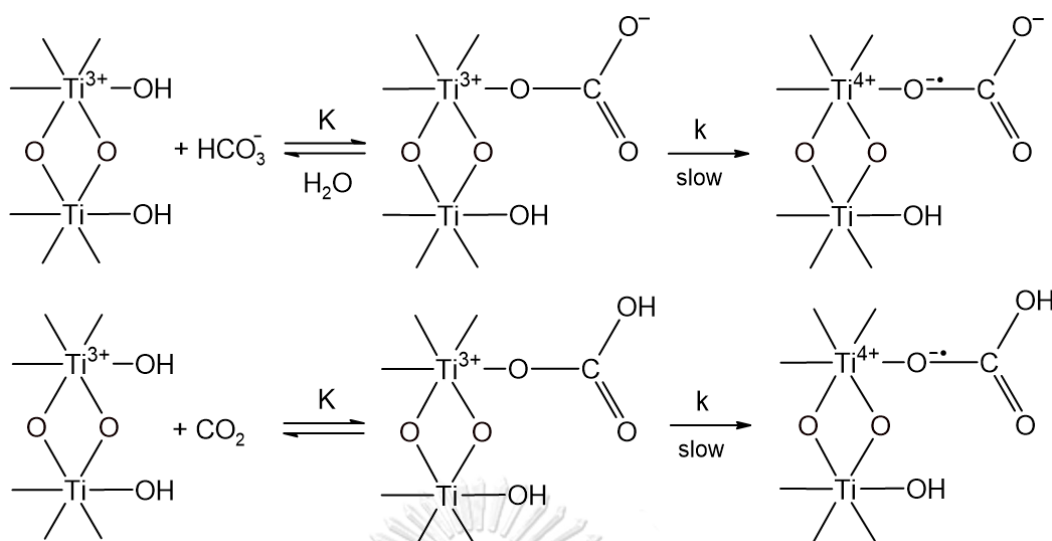
Figure 22 Adsorption equilibrium (K) and the rate constant of radical anion formation (k) for bicarbonate and carbon dioxide [83].

$$CO_{2(aq)} + 8H^+_{(aq)} + 8e^- \longrightarrow CH_{4\,(g)} + H_2O_{(l)} \qquad\qquad \text{Eq. 53}$$

$$\text{Rate} = d[CO_2]_w/dt = 1/8\,d[H^+]/dt = kK[CO_2]_w/(1 + K[CO_2]_w) \qquad \text{Eq. 54}$$

Eq. 53 shows overall reaction to produce one molecule of CH_4, from CO_2; 8 moles of e^- and 8 electrons of H^+ in photoreduction are consumed. However, CO_2 or HCO_3^- adsorption on TiO_2 as Figure 22 shows must occur before CO_2 or HCO_3^- further reduction. Langmuir-Hinshelwood (LH) is an approach that could be used as a kinetic model. According to Eq. 54, the equilibrium constant of HCO_3^- adsorption (K) and the rate constant of CH_4 formation (k) at maximum adsorbed HCO_3^- on TiO_2 surface (HCO_3^--TiO_2) can be obtained from the production rate results under different pH conditions. At the range of pH 5.29-7.29 used HCO_3^- is the main species in solution [7], meanwhile, TiO2 surface charge changes in this pH range. TiO_2 surface is mainly positive (+) charge at pH 5.29, neutral or zero (0) charge at pH 6.29 and negative charge (-) at pH 7.29. Therefore, the constant values of k and K for the kinetic model under each TiO_2 charge surfaces can be obtained under different initial concentrations. The CH_4 rate formation under $[HCO_3^-]_0 = 11.9$-$71.4\ 34$ μmole/ml_{H2O} at each pH 5.29-7.29 are showed in Figure 23. According to Eq. 54, the k and K values were obtained from the

plot of 1/rate versus $1/[HCO_3^-]_0$, as shown in Figure 24, which $1/Kk = k_{obs}$ values were obtained from line slopes and $1/k$ from the intercept.
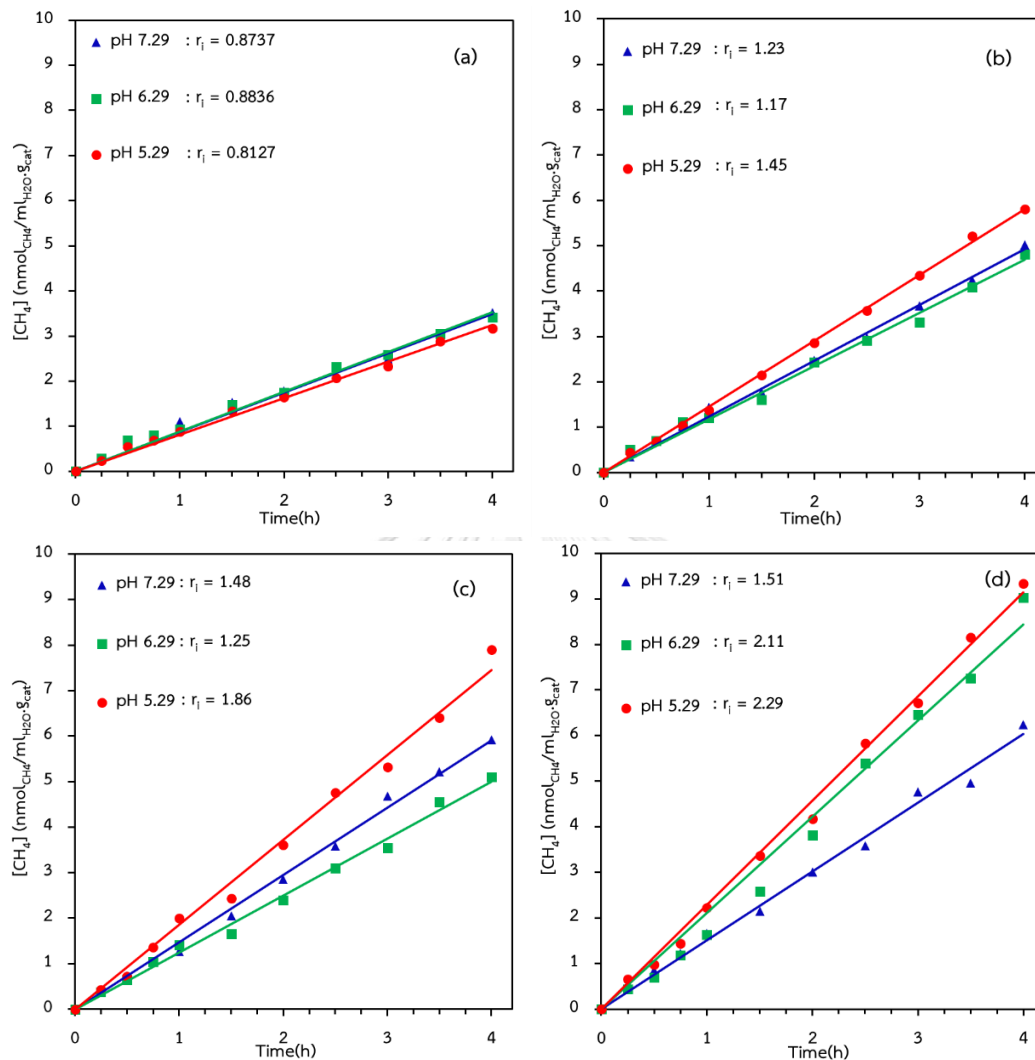
Figure 23 [CH$_4$] versus t plots obtained in the P25 photoreduction of $[HCO_3^-]_0 =$ (a) 11.9, (b) 23.8, (c) 47.6 and (d) 71.4 *34* µmole/ml at temperature 45 °C.
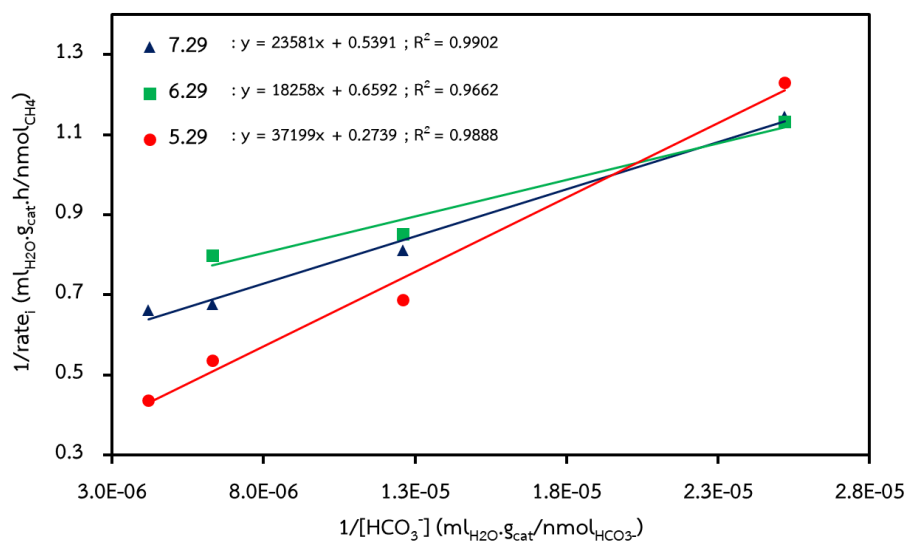
Figure 24 Plots of 1/rate Vs $1/[HCO_3^-]_0$ at different pH.

Table 7 CH_4 formation rates at different pH and $[HCO_3^-]_0$, Obtained Kk=kobs, K and k values from Figure 24 and % CH_4 conversion.

pH	$[HCO_3^-]_0$ (μmol/ml$_{H2O}$)								$kK \times 10^5$ (h^{-1})	k (nmol/ml$_{H2O}$·g$_{cat}$.h)	$K \times 10^5$ (ml$_{H2O}$·g$_{cat}$/nmol)
	11.9	23.8	47.6	71.4	11.9	23.8	47.6	71.4			
	rate$_i$ (nmol/ml$_{H2O}$·g$_{cat}$.h)				% CH_4 conversion x 10^3						
7.29	0.87	1.23	1.48	1.51	7.56	5.35	3.11	2.11	4.24	1.85	2.29
6.29	0.88	1.17	1.25	2.11	7.65	5.09	2.63	2.95	5.48	1.52	3.61
5.29	0.81	1.45	1.86	2.29	7.04	6.30	3.91	3.21	2.69	3.65	0.74

The equilibrium constant of HCO_3^- adsorption (K) and the rate constant of CH_4 formation (k) change according to charge surface types of TiO_2 at pH used (pH = 5.29(+), 6.29(0) and 7.29(-)). The trend of adsorption constant are K(0) > K(-) > K(+) and the rate constant of CH_4 formation are k(+) > k(-) > k(0). In Figure 25, the relative stabilities of TiO_2-HCO_3^- adduct and the radical anion formation at the neutral, positive and negative charge surface are shown. The HCO_3^- is better adsorbed on the neutral charge surface (0) than in the negative charged surface (-), due to negative charges repulsion at the negative site of HCO_3^- [84]. Meanwhile, the HCO_3^- adsorbs less on positive charged surface, as expected since bicarbonate is attacked from the H_2O^+, a poor nucleophile [85].

On the contrary, the rate constant of CH_4 formation (k) that involves e^- transfer to form radical anion, was favoured on the positive charged surface. It indicates that the electrostatic interaction between H_2O^+ stabilizes the radical anion formation HCO_3^-. However, the radical anion formation was better stabilized on the negative charge surface when compare to the neutral charge surface, due to delocalization occur and form the di-anionic [86]. These HCO_3^- photoreduction results could be concluded that the neutral charged surface was more effective when considering the k_{obs} (kK) value. Although the positive charged surface (pH = 5.29) provide faster electron transfer rate, it provide the lowest adsorption efficiency.
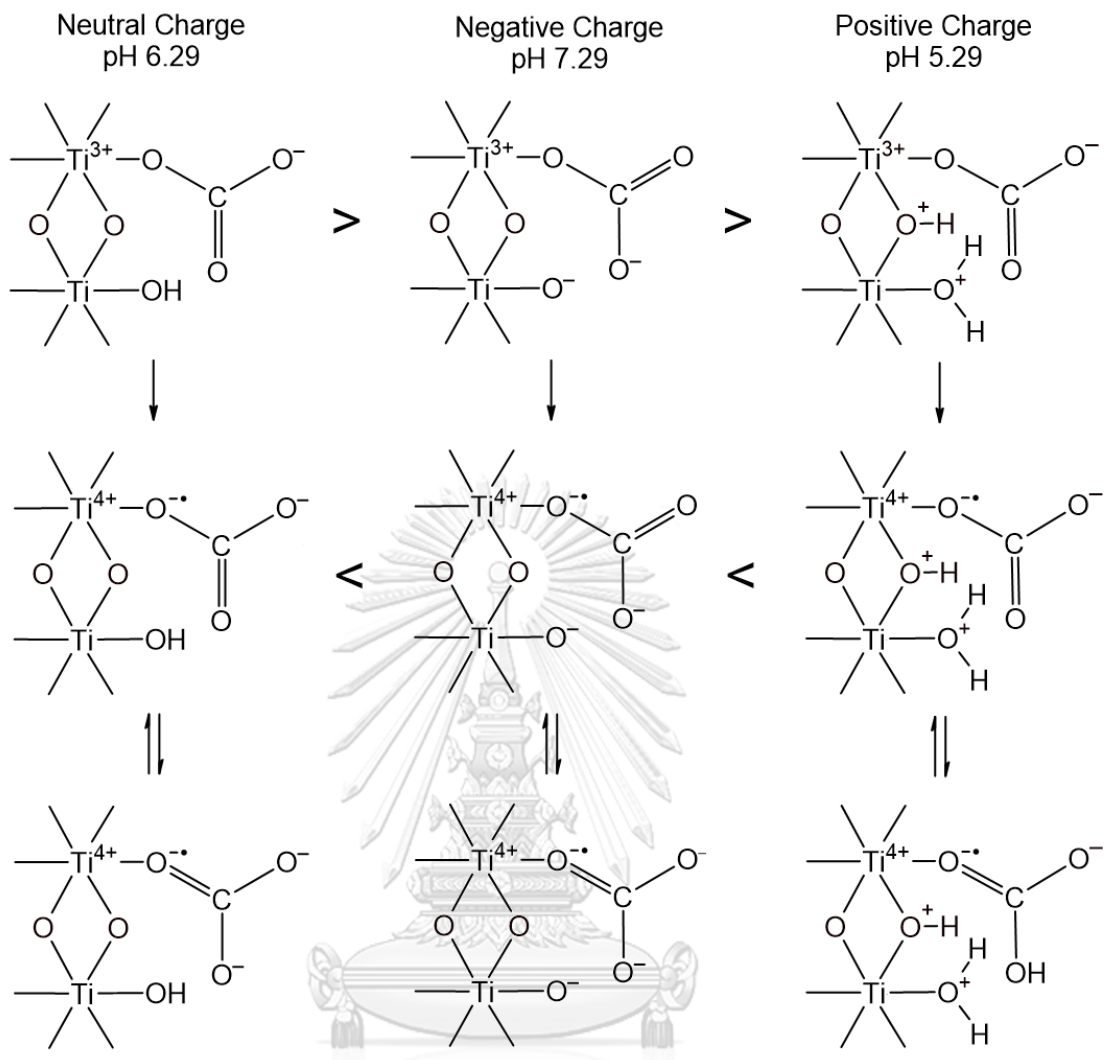
Figure 25 TiO_2-HCO_3^- adducts and corresponding radical anions relative stabilities at neutral, positive and negative charged TiO_2 surface [84, 85] .

4.4 Changing P-25 morphology

It has been reported [84] that the morphology of catalyst affects the photoactivity. For P25 catalyst, using only one phase whether it be anatase or rutile phase it exhibited low activity. However, the coupling between 2 phases can improve the activity of photoreaction and get higher yield of products. A cooperative performance is then expected. The coupling phases in TiO_2 may be promoted by the sonication of P25 [87]. Under the same condition ($[HCO_3^-]_0$ = 71.4 x 10^3 nmol/ml_{H2O}, pH = 5.29 and temperature 45 °C). As shown in Figure 26 CH_4 formation rate using original P25 catalyst (P25) is 2.80 nmol/$ml_{H2O}g_{cat}$h. The sonicated P25 catalyst (Sonic.P25) has about 4 times faster rate and CH_4 selectivity is also increased as shown in the [CO]/[CH_4] plot (Figure 27). Although the [CO]/[CH_4] of P25 and Sonic.P25 were similar at the beginning time (t_0), [CO]/[CH_4] of P25 increases with time, while the [CO]/[CH_4] of Sonic.P25 is steady. This means that the Sonic.P25 does not have another alternative pathway that produces more CO as when original P25 is used. It is proposed that Sonic.P25 performed only by the main mechanism (Fig. 19) to produce products without the involvement of oxygen vacancies (O_V) which lead to more CO production. Regularly, the O_V act as the e^- trap that inhibits the e^-/h^+ recombination but the O_V can detain the e^- in the trap steadily and delay the e- transfer the electrolyte. In the one phase performance (Figure 20), the O_V preferentially direct e^- to reduce reactant and to fulfill the oxygen in vacancies. This oxygen replenishment leads to more CO production. After sufficient replenishment, the alternative formation path as Figure 20 will return to the normal path as Figure 19. On the other hand, the O_V in Sonic.P25 provides a superior photoactivity. In addition to the co-working of narrow bandgap between anatase and rutile phases cause better electron hierarchical transfer, the O_V in the coupling between phases reduces recombination and promote electron transfer from anatase conduction band. In addition to the co-working of narrow bandgap between anatase and rutile phases cause better electron hierarchical transfer. The e^-

of rutile phase move to anatase Ov from where it combines with anatase phase hole (h^+); therefore, anatase excited e^- can be transfer to the electrolyte faster since its recombination with its hole is minimized, as shown in Figure 28. This effect explains the faster CH_4 formation rate and its selectivity increment.

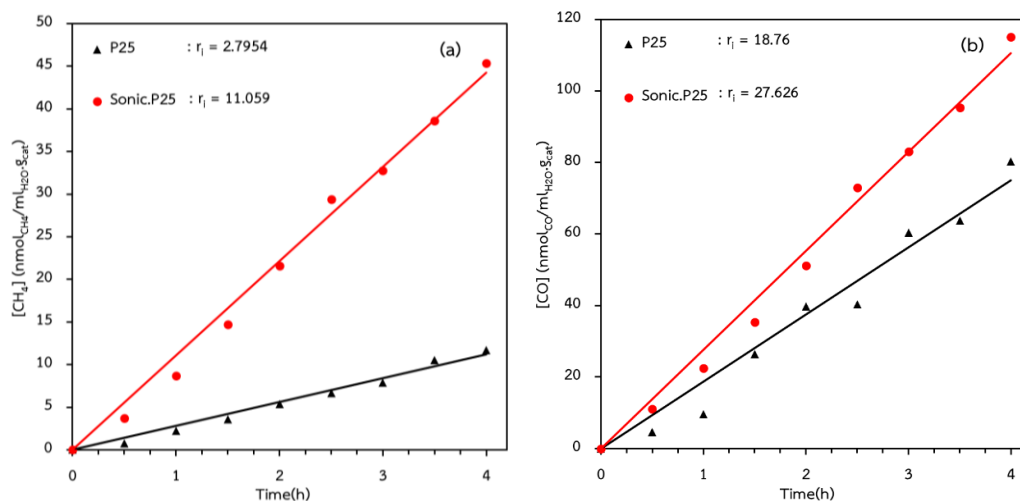**Figure 26** (a). CH_4 and (b). CO formation rate of HCO_3^- photoreduction on the P25 and Sonic.P25 catalysts under $[HCO_3^-]_0$ = 71.4 µmol/ml and pH 5.29.
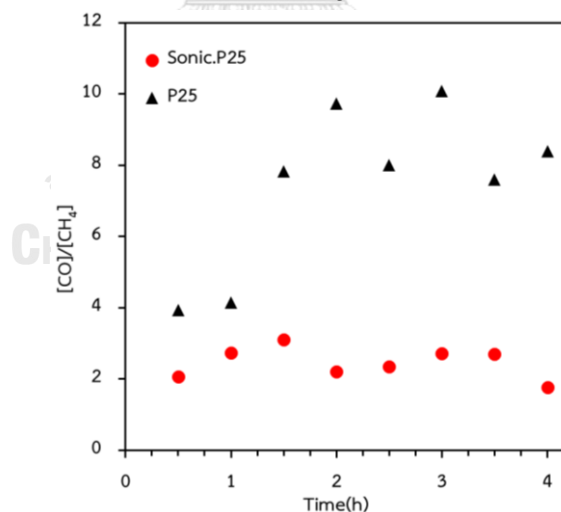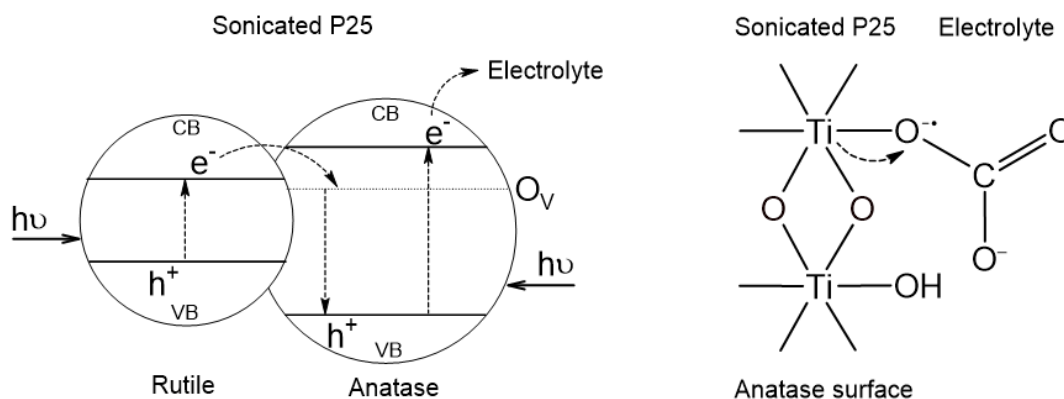

Figure 27 [CO]/[CH_4] versus time plots of produced products concentration from HCO_3^- photoreduction on the P25 and Sonic.P25 catalysts.

Figure 28 The electron transfer to the electrolyte in the coupling narrow band gap between anatase and rutile phases and its oxygen vacancy

4.5 [CO]/[CH$_4$] ratios and alternative CO pathway formation

The [CO]/[CH$_4$] ratios versus time plots are shown in Figure 19 and 29. [CO]/[CH$_4$] ratios increase at the beginning period with a further stabilization (fulfill oxygen vacancy). There is just one mechanism pathway for CH$_4$ and CO formation if the ratio is constant with reaction time. However, if there is CH$_4$ and CO equilibrium or if there is an alternative pathway, ratio changed with time. From the ratio plots of Figure 29, it increased in the beginning period and decreased after 2 hours of reaction time. Therefore, the alternative pathway was causing the changing of [CO]/[CH$_4$] ratios. The straight line intersection ratio at t=0 were the [CO]/[CH$_4$] ratio without an alternative pathway. Furthermore, the [CO]/[CH$_4$] ratio increases faster at lower pH condition. This means that the acid condition could promote the CO alternative pathway, just as it is indicated in Figure 20 (bottom).

As shown in Figure 20, the interaction of O$_V$ with HCO$_3^-$-TiO$_2$ may produce CO by fulfill O$_V$ as reported for CO$_2$ case [88]. The O$_V$ occupation in the alternative pathway may deactivate the activity of P25. However, the P25 activity could be reactivated by creating new O$_V$ during photocatalytic reduction.
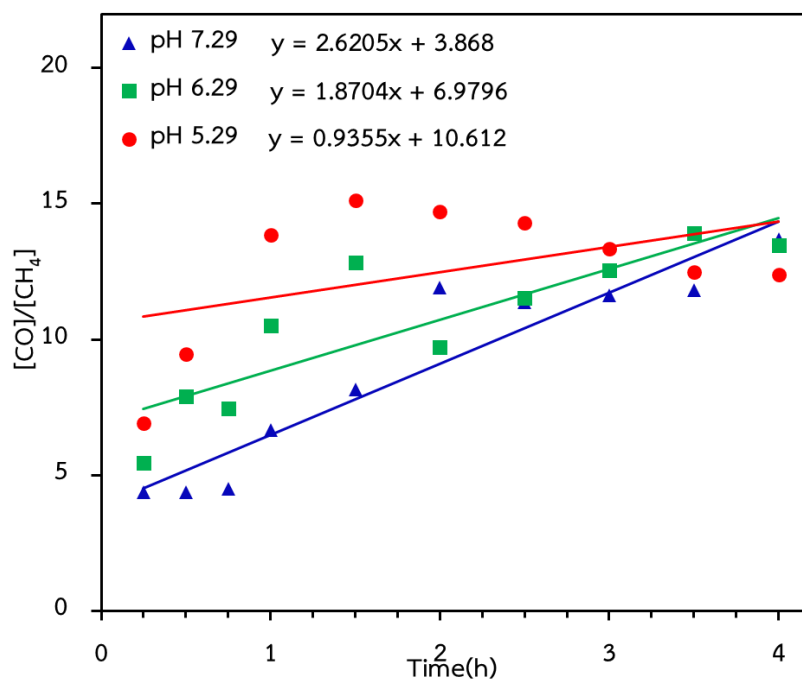
Figure 29 The $[CO]/[CH_4]$ ratio versus time plot obtained by HCO_3^- photoreduction on P25 catalyst under UV irradiation, temperature $45\,^{\circ}C$, $[HCO_3^-]_0 = 23.8$ **μ**mol/ml at three different pH.

4.6 H_2O/D_2O solvent isotope effect

H_2O is an important solvent for HCO_3^- photoreduction since it provides protons required. Solvent isotope effects were studied to prove the importance and possibility of solvent in the rate limiting step of photoreduction. The solvent isotope effect can be observed by changing the used isotope solvent from H_2O to D_2O. Changing the transfer of H to D in the rate limiting step, as shown in Figure 31. Isotope change may also affect the equilibrium for adduct formation since it shifted to the left when using D_2O because OD^- is more basic than OH^- about two times. Likewise, the LCO_3^- substrate promote changing of the equilibrium K when DCO_3^- and HCO_3^- are used [89], balancing the equilibrium isotope change. Therefore, the transfer of protons L^+ from L_2O in rate-limiting step may be the main contribution to the the solvent isotope effect observed. From the experimental results, the solvent isotope effect can be determined by comparing the product rate of CH_4, CO and H_2 when using H_2O and D_2O as solvent.

KIEs = rate$_{H2O}$/rate$_{D2O}$ = k$_{obs}$(H$_2$O)/k$_{obs}$(D$_2$O) = 1.38 for CH$_4$, 1.4 for CO and H$_2$ formation are obtained. The experiment is operated on P25 under the negative charge surface condition (pH > 7.5). Therefore, L transfer at the transition state (e$^-$ transfer step) must come from water. The obtained KIEs are not larger due to L position in L$_2$O donor, and C=O acceptor is not symmetric. The small solvent isotope effect observed for H$_2$ formation indicates that L$^+$ reduction to L$_2$ on the TiO$_2$ surface is minimum in the photoreduction [90].
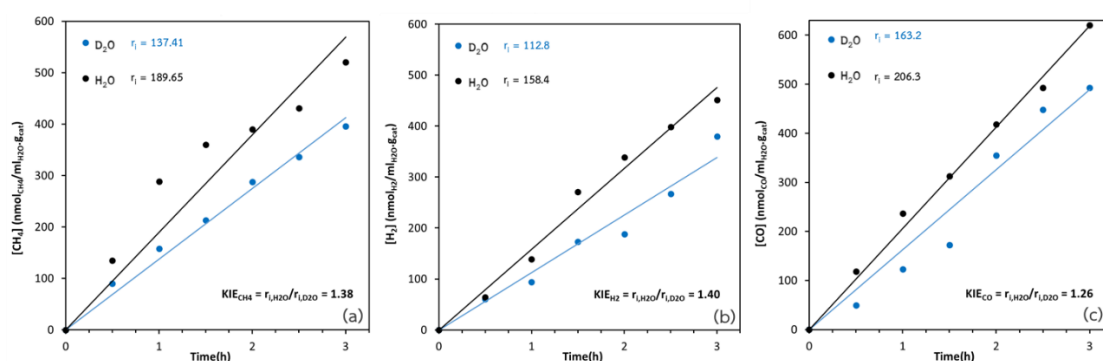
Figure 30 Solvent H$_2$O/D$_2$O isotope effect in the rates of (a) CH$_4$, (b) H$_2$ and (c) CO formation from HCO$_3^-$ photoreduction on P25 under UV irradiation, [HCO$_3^-$]$_0$ = 23.8 μmol/ml, Temperature 45 °C.
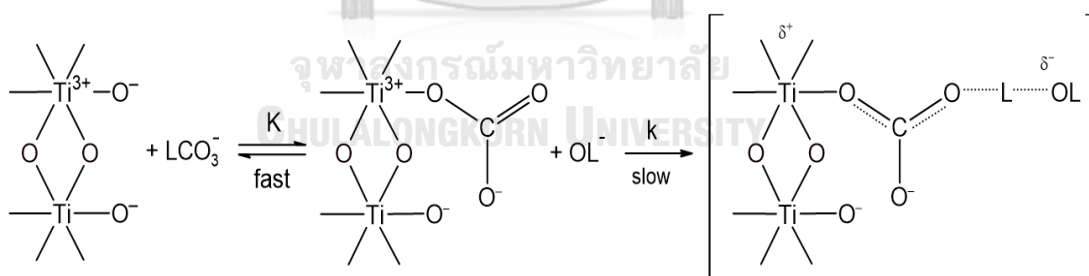
Figure 31 Solvent isotope effect at the equilibrium (K) and transition state (k) of products common intermediate (radical anion) formation.

# CHAPTER V

CONCLUSION AND RECOMMENDATION

5.1 Conclusion

CO_2 photoreduction in aqueous phase on P25 (TiO_2) operated under UV light irradiation produces 9% CH_4, 65% CO, 25% H_2 and 1% CH_3OH with very low conversion 7×10^3 % for CH_4. The production rates are limited by TiO_2-CO_2 adduct radical anion intermediate formation. Partitioning of this intermediate produces CH_4 and CH_3OH through carbene intermediate path; meanwhile, CO and H_2 are also produced from the same radical anion partitioning. $[CO]/[CH_4]$ and $[H_2]/[CH_4]$ ratios plot increase with time, therefore there is an alternative path at O_V in P25, which promote CO and H_2 production that decreases CH_4 selectivity. The O_V can be produced by TiO_2 self-oxidation in VB. HCO_3^- photoreduction has same rate limiting step as CO_2 and proceeds through a mechanism via LH mechanism. In the same conditions, the production rate when using HCO_3^- as the reactant is faster than when using CO_2. Bicarbonate adsorption equilibrium to form TiO_2-HCO_3^- is larger due to the hybridization change from sp to sp^2 in CO_2 case. LH kinetic model allows to obtain, K and k values depending on the charge surface species of TiO_2, which can be controlled by changing pH conditions: positive (+, pH 5.29), neutral (0, pH 6.29) and negative (-, pH 7.29) charge surfaces. The trend of the adsorption equilibrium constant is K(0) > K(-) > K(+) and the rate constant k is k(+) > k(-) > k(0). It means that HCO_3^- adsorbs better on the neutral and negative charge surface; meanwhile the positive charge surface attack HCO_3^- inhibits adduct formation. As opposed to the electron transfer rate (k) is favored in low pH condition due to stability of formed radical anion on the positive charge surface. The $[CO]/[CH_4]$ and $[H_2]/[CH_4]$ ratios in the HCO_3^- photoreduction increase at the initial period, meaning that more CO and H_2 are produced by an alternative pathway via O_V. The solvent isotope effect, KIEs value of $rate_{H2O}/rate_{D2O} = 1.4$ is observed for CH_4, and CO and H_2

formation. It confirms that the radical anion adduct formation is a common rate limiting step for all products detected in the photoreduction.

Low absorption on P25 can be improved by increasing pH condition. However, the e^-/h^+ recombination in anatase phase inhibits the electron transfer to the electrolyte, and its O_V tends to decrease CH_4 selectivity.   Sonicated P25 increases the production rate and selectivity of CH_4, since loading anatase on the rutile phase promotes reactants adsorption and charge separation and reduce trapped electron from O_V to be transferred to the electrolyte.

5.2 Recommendation

1. Develop a process for continuous flow.

2. Using other buffers that can accelerate the photocatalytic reaction.
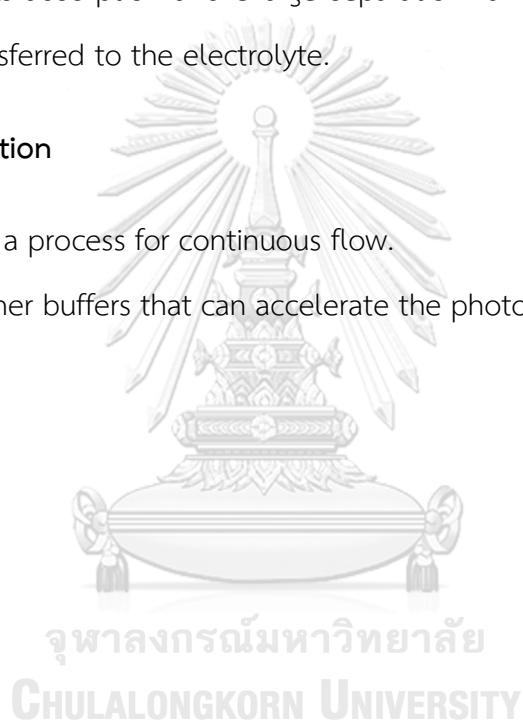
REFERENCES

1. Chang, X., T. Wang, and J. Gong, CO_2 photo-reduction: insights into CO_2 activation and reaction on surfaces of photocatalysts. Energy & Environmental Science, 2016. 9(7): p. 2177-2196.

2. Hong, J., et al., Photocatalytic reduction of CO_2: a brief review on product analysis and systematic methods. Analytical Methods, 2013. 5(5): p. 1086-1097.

3. Lin, W., H. Han, and H. Frei, CO_2 Splitting by H_2O to CO and O_2 under UV Light in TiMCM-41 Silicate Sieve. The Journal of Physical Chemistry B, 2004. 108(47): p. 18269-18273.

4. János, R. and F. Solymosi, Infrared Spectroscopic Study of the Photoinduced Activation of CO_2 on TiO_2 and Rh/TiO_2 Catalysts. The Journal of Physical Chemistry, 1994. 98: p. 7147-7152.

5. Fertig, M., Finite Rate Surface Catalysis Modelling of PM1000 and SiC Employing the DLR CFD Solver TAU. 2015.

6. He, X., et al., Rapid Formation of Metal–Organic Frameworks (MOFs) Based Nanocomposites in Microdroplets and Their Applications for CO_2 Photoreduction. ACS Applied Materials & Interfaces, 2017. 9(11): p. 9688-9698.

7. Takahashi, T. and S. Yokoyama, Bioassay of Components Eluted from Electric Arc Furnace Steel Slag Using Microalgae Chlorella. ISIJ International, 2016. 56: p. 1497–1505.

8. Pan, H., et al., Efficient production of formic acid by simultaneous photoreduction of bicarbonate and oxidation of glycerol on gold-TiO_2 composite under solar light. Journal of CO_2 Utilization, 2017. 22: p. 117-123.

9. Kumar, K.V., K. Porkodi, and F. Rocha, Langmuir–Hinshelwood kinetics – A theoretical study. Catalysis Communications, 2008. 9(1): p. 82-84.

10. Nuñez, O., et al., Unprecedented large solvent (H_2O vs. D_2O) isotope effect in semiconductors photooxidation. Journal of Physical Organic Chemistry, 2019. 32.

11. Li, K., et al., A critical review of CO_2 photoconversion: Catalysts and reactors. Catalysis Today, 2014. 224: p. 3-12.

12. Park, H., et al., Surface modification of TiO_2 photocatalyst for environmental applications. Journal of Photochemistry and Photobiology C: Photochemistry Reviews, 2013. 15: p. 1-20.

13. Wang, W.-N., Comparison of CO_2 Photoreduction Systems: A Review. Aerosol and Air Quality Research, 2014.

14. Viswanathan, K.R.V.J.K.R.K.B., Photocatalytic reduction of carbon dioxide by water on titania: Role of photophysical and structural properties. Indian Journal of Chemistry, 2012. 51 A: p. 411-419.

15. Ungan, H. and T. Tekin, Effect of the sonication and coating time on the photocatalytic degradation of TiO2, TiO_2- Ag, and TiO_2- ZnO thin film photocatalysts. Chemical Engineering Communications, 2019: p. 1-8.

16. Le Quéré, C., et al., Global Carbon Budget 2018. Earth System Science Data, 2018. 10(4): p. 2141-2194.

17. David Wei, W., et al., Current Development of Photocatalysts for Solar Energy Conversion, in New and Future Developments in Catalysis. 2013. p. 279-304.

18. Abdullah, H., et al., Modified TiO_2 photocatalyst for CO_2 photocatalytic reduction: An overview. Journal of CO_2 Utilization, 2017. 22: p. 15-32.

19. Ohtani, B., Photocatalysis A to Z—What we know and what we do not know in a scientific sense. Journal of Photochemistry and Photobiology C: Photochemistry Reviews, 2010. 11(4): p. 157-178.

20. Tahir, M. and N.S. Amin, Advances in visible light responsive titanium oxide-based photocatalysts for CO_2 conversion to hydrocarbon fuels. Energy Conversion and Management, 2013. 76: p. 194-214.

21. Molinari, R., P. Argurio, and C. Lavorato, Photocatalytic hydrogenation of organic compounds in membrane reactors, in Membrane Reactors for Energy Applications and Basic Chemical Production. 2015. p. 605-639.

22. Emeline, A.V., et al., Heterogeneous Photocatalysis: Basic Approaches and Terminology, in New and Future Developments in Catalysis. 2013. p. 1-47.

23. Al-Mamun, M.R., et al., Photocatalytic activity improvement and application of UV-TiO_2 photocatalysis in textile wastewater treatment: A review. Journal of Environmental Chemical Engineering, 2019. 7(5).

24. Tri Wahyuni, E. and N. Hidayat Aprilita, Photoreduction Processes over TiO_2 Photocatalyst, in Photocatalysts - Applications and Attributes. 2019.

25. Khalid, N. R., et al., Highly visible light responsive metal loaded N/TiO_2 nanoparticles for photocatalytic conversion of CO_2 into methane. Ceramics International, 2017. 43(9): p. 6771-6777.

26. Ola, O. and M. M. Maroto-Valer, Review of material design and reactor engineering on TiO_2 photocatalysis for CO_2 reduction. Journal of Photochemistry and Photobiology C: Photochemistry Reviews, 2015. 24: p. 16-42.

27. Dambournet, D., I. Belharouak, and K. Amine, Tailored Preparation Methods of TiO_2 Anatase, Rutile, Brookite: Mechanism of Formation and Electrochemical Properties†. Chemistry of Materials, 2010. 22(3): p. 1173-1179.

28. Oi, L. E., et al., Recent advances of titanium dioxide (TiO_2) for green organic synthesis. RSC Advances, 2016. 6(110): p. 108741-108754.

29. Luttrell, T., et al., Why is anatase a better photocatalyst than rutile?--Model studies on epitaxial TiO_2 films. Sci Rep, 2014. 4: p. 4043.

30. Zhao, H., et al., Bicrystalline TiO_2 with controllable anatase–brookite phase content for enhanced CO_2 photoreduction to fuels. Journal of Materials Chemistry A, 2013. 1(28).

31. Fang, W., et al., Reduced {001}-TiO_2-x photocatalysts: noble-metal-free CO_2 photoreduction for selective CH_4 evolution. Phys Chem Chem Phys, 2017. 19(21): p. 13875-13881.

32. Yan, H., et al., Band structure design of semiconductors for enhanced photocatalytic activity: The case of TiO_2. Progress in Natural Science: Materials International, 2013. 23(4): p. 402-407.

33. Chen, X. and F. Jin, Photocatalytic reduction of carbon dioxide by titanium oxide-based semiconductors to produce fuels. Frontiers in Energy, 2019. 13(2): p. 207-220.

34. Gao, A., et al., The Symmetric Exchange Reaction OH + H_2O --> H_2O + OH: Convergent Quantum Mechanical Predictions. J Phys Chem A, 2016. 120(51): p. 10223-10230.

35. Matsubara, Y. , D. C. Grills, and Y. Kuwahara, Thermodynamic Aspects of Electrocatalytic CO_2 Reduction in Acetonitrile and with an Ionic Liquid as Solvent or Electrolyte. ACS Catalysis, 2015. 5(11): p. 6440-6452.

36. Mackenzie, J.W.M.F.T., Chapter 1 The CO_2-Carbonic Acid System and Solution Chemistry, in Geochemistry of Sedimentary Carbonates. 1990. p. 1-38.

37. Liu, L. and Y. Li, Understanding the Reaction Mechanism of Photocatalytic Reduction of CO_2 with H_2O on TiO_2-Based Photocatalysts: A Review. Aerosol and Air Quality Research, 2014. 14(2): p. 453-469.

38. Molinari, A., L. Samiolo, and R. Amadelli, EPR spin trapping evidence of radical intermediates in the photo-reduction of bicarbonate/CO_2 in TiO_2 aqueous suspensions. Photochem Photobiol Sci, 2015. 14(5): p. 1039-46.

39. Menéndez, J.A., et al., On the difference between the isoelectric point and the point of zero charge of carbons. Carbon, 1995. 33(11): p. 1655-1657.

40. Nakata, K. and A. Fujishima, TiO_2 photocatalysis: Design and applications. Journal of Photochemistry and Photobiology C: Photochemistry Reviews, 2012. 13(3): p. 169-189.

41. Veronovski, N., TiO_2 Applications as a Function of Controlled Surface Treatment, in Titanium Dioxide - Material for a Sustainable Environment. 2018.

42. Beranek, R., (Photo)electrochemical Methods for the Determination of the Band Edge Positions of TiO_2-Based Nanomaterials. Advances in Physical Chemistry, 2011. 2011: p. 1-20.

43. Beranek, R., (Photo)electrochemical Methods for the Determination of the Band Edge Positions of TiO_2-Based Nanomaterials. Advances in Physical Chemistry, 2011. DOI:10.1155/2011/786759.

44. Bahadori, E. , et al., High Pressure Photoreduction of CO_2: Effect of Catalyst Formulation, Hole Scavenger Addition and Operating Conditions. Catalysts, 2018. 8(10).

45. Roldan, A. , et al., Bio-inspired CO_2 conversion by iron sulfide catalysts under sustainable conditions. Chem Commun (Camb), 2015. 51(35): p. 7501-4.

46.   Bai, Y., et al., Engineering the surface charge states of nanostructures for enhanced catalytic performance. Materials Chemistry Frontiers, 2017. 1(10): p. 1951-1964.

47.   Chen, D., X. Zhang, and A.F. Lee, Synthetic strategies to nanostructured photocatalysts for CO_2 reduction to solar fuels and chemicals. Journal of Materials Chemistry A, 2015. 3(28): p. 14487-14516.

48.   Poulios, I., et al., Photooxidation of eosin Y in the presence of semiconducting oxides. Applied Catalysis B: Environmental, 2003. 41(4): p. 345-355.

49.   Janak, K., D. Churchill, and G. Parkin, Kinetic and Equilibrium Deuterium Isotope Effects for C—H Bond Reductive Elimination and Oxidative Addition Reactions Involving the Ansa—Tungstenocene Methyl—Hydride Complex [Me 2 Si(C 5 Me 4) 2]W(Me)H. ACS Symp. Ser., 2004. 885.

50.   CHAPTER 8 - Isotope Effects, in Studies in Organic Chemistry, F. Ruff and I.G. Csizmadia, Editors. 1994, Elsevier. p. 210-256.

51.   Aseman, M.D., et al., Secondary Kinetic Isotope Effects in Oxidative Addition of Benzyl Bromide to Dimethylplatinum(II) Complexes. Organometallics, 2013. 32(9): p. 2593-2598.

52.   Petralia, L.S., et al., Strong inverse kinetic isotope effect observed in ammonia charge exchange reactions. Nature Communications, 2020. 11(1): p. 173.

53.   Shiner, V.J., M.W. Rapp, and H.R. Pinnick, .alpha.-Deuterium effects in SN2 reactions with solvent. Journal of the American Chemical Society, 1970. 92(1): p. 232-233.

54.   Ma, H., et al., Pd(ii)/Ag(i)-Cocatalyzed ortho direct arylation of O-phenylcarbamates with pinacol aryl boronates. Organic Chemistry Frontiers, 2019. 6(9): p. 1409-1413.

55.   Honda, T.I.A.F.S.H.K., Photoelectrocatalytic reduction of carbon dioxide in aqueous suspensions of semiconductor powders. Nature, 1979. 277: p. 637-638.

56.   Kavil, Y.N., et al., Photocatalytic conversion of CO_2 into methanol over Cu-C/TiO_2 nanoparticles under UV light and natural sunlight. Journal of Photochemistry and Photobiology A: Chemistry, 2017. 347: p. 244-253.

57. KoČĺ, K., et al., Wavelength Effect on Photocatalytic Reduction of CO_2 by Ag/TiO_2 Catalyst. Chinese Journal of Catalysis, 2011. 32(5): p. 812-815.

58. Kim, W. , T. Seok, and W. Choi, Nafion layer- enhanced photosynthetic conversion of CO_2 into hydrocarbons on TiO_2 nanoparticles. Energy & Environmental Science, 2012. 5(3).

59. Wu, T.S., et al., Enhancement of catalytic activity by UV-light irradiation in CeO_2 nanocrystals. Sci Rep, 2019. 9(1): p. 8018.

60. Matsumura, T.O.K.S.K.T.M., Morphology of a TiO_2 Photocatalyst (Degussa, P-25) Consisting of Anatase and Rutile Crystalline Phases. Journal of Catalysis, 2001. 203: p. 82-86.

61. Tsukamoto, D. , et al. , Gold Nanoparticles Located at the Interface of Anatase/Rutile TiO_2 Particles as Active Plasmonic Photocatalysts for Aerobic Oxidation. Journal of the American Chemical Society, 2012. 134(14): p. 6309-6315.

62. Birkholz, M., P. Fewster, and C. Genzel, Thin Film Analysis by X-ray Scattering. Vol. 58. 2005.

63. Thirugnanasambandan, T. and M. Alagar, Titanium dioxide (TiO_2) Nanoparticles XRD Analyses: An Insight. arXiv:1307.1091 (http://arxiv.org/abs/1307.1091), 2013. JOURNAL CITATION: arXiv:1307.1091.

64. Gubicza, J., et al., Particle size distribution and dislocation density determined by high resolution X- ray diffraction in nanocrystalline silicon nitride powders. Materials Science and Engineering: A, 2000. 280(2): p. 263-269.

65. Krishnan, P., et al., Characterization of photocatalytic TiO_2 powder under varied environments using near ambient pressure X- ray photoelectron spectroscopy. Scientific Reports, 2017. 7(1): p. 43298.

66. Zuo, F., et al., Self-Doped Ti^{3+} Enhanced Photocatalyst for Hydrogen Production under Visible Light. Journal of the American Chemical Society, 2010. 132(34): p. 11856-11857.

67. Wang, C., et al., Design of Superior Ethanol Gas Sensor Based on Al-Doped NiO Nanorod-Flowers. ACS Sensors, 2016. 1(2): p. 131-136.

68. Jiang, X., et al., Characterization of Oxygen Vacancy Associates within Hydrogenated TiO_2: A Positron Annihilation Study. The Journal of Physical Chemistry C, 2012. 116(42): p. 22619-22624.

69. Kočí, K., et al., Effect of TiO_2 particle size on the photocatalytic reduction of CO_2. Applied Catalysis B-environmental - APPL CATAL B-ENVIRON, 2009. 89: p. 494-502.

70. Rawal, S.B., et al., Design of visible-light photocatalysts by coupling of narrow bandgap semiconductors and TiO_2: effect of their relative energy band positions on the photocatalytic efficiency. Catalysis Science & Technology, 2013. 3(7): p. 1822-1830.

71. Nolan, M., Electronic coupling in iron oxide-modified TiO_2 leads to a reduced band gap and charge separation for visible light active photocatalysis. Physical Chemistry Chemical Physics, 2011. 13(40): p. 18194-18199.

72. Yan, J., et al., Understanding the effect of surface/bulk defects on the photocatalytic activity of TiO_2: anatase versus rutile. Physical Chemistry Chemical Physics, 2013. 15(26): p. 10978-10988.

73. Baoshun, L., L. Wen, and X. Zhao, The photoluminescence spectroscopic study of anatase TiO_2 prepared by magnetron sputtering. Materials Chemistry and Physics, 2007. 106: p. 350-353.

74. Tan, S.S. and L. Zou, Photocatalytic reduction of carbon dioxide into gaseous hydrocarbon using TiO_2 pellets. Catalysis Today, 2006. 115: p. 269-273.

75. Akhter, P., et al., Novel nanostructured-TiO_2 materials for the photocatalytic reduction of CO_2 greenhouse gas to hydrocarbons and syngas. Fuel, 2015. 149: p. 55-65.

76. Liu, L. and Y. Li, Understanding the Reaction Mechanism of Photocatalytic Reduction of CO_2 with H_2O on TiO_2-Based Photocatalysts: A Review. Aerosol and Air Quality Research, 2014. 14: p. 453-469.

77. Nahar, S., et al., Advances in Photocatalytic CO_2 Reduction with Water: A Review. Materials (Basel, Switzerland), 2017. 10(6): p. 629.

78. Pan, X., et al., Defective TiO_2 with oxygen vacancies: synthesis, properties and photocatalytic applications. Nanoscale, 2013. 5(9): p. 3601-3614.

79. Molinari, A., L. Samiolo, and R. Amadelli, EPR spin trapping evidence of radical intermediates in the photo-reduction of bicarbonate/CO_2 in TiO_2 aqueous suspensions. Photochemical & Photobiological Sciences, 2015. 14(5): p. 1039-1046.

80. Leonard, D. P., H. Pan, and M. D. Heagy, Photocatalyzed Reduction of Bicarbonate to Formate: Effect of ZnS Crystal Structure and Positive Hole Scavenger. ACS Applied Materials & Interfaces, 2015. 7(44): p. 24543-24549.

81. Chen, S. and G. Cao, Study on the photocatalytic reduction of dichromate and photocatalytic oxidation of dichlorvos. Chemosphere, 2005. 60(9): p. 1308-1315.

82. Colón, G., M.C. Hidalgo, and J. Navío, Photocatalytic deactivation of commercial TiO_2 samples during simultaneous photoreduction of Cr(VI) and photooxidation of salicylic acid. Journal of Photochemistry and Photobiology A-chemistry - J PHOTOCHEM PHOTOBIOL A-CHEM, 2001. 138: p. 79-85.

83. Yui, T., et al., Photochemical Reduction of CO_2 Using TiO_2: Effects of Organic Adsorbates on TiO_2 and Deposition of Pd onto TiO_2. ACS Applied Materials & Interfaces, 2011. 3(7): p. 2594-2600.

84. Sharma, S.K., Heavy Metals In Water: Presence, Removal and Safety. 2014: Royal Society of Chemistry.

85. Zheng, Y., et al., Carbon Dioxide Reduction through Advanced Conversion and Utilization Technologies. 2019: CRC Press.

86. Song, X., et al., Anionic Dopant Delocalization through p-Band Modulation to Endow Metal Oxides with Enhanced Visible-Light Photoactivity. Angewandte Chemie International Edition, 2019. 58(46): p. 16660-16667.

87. Abdullah, H., et al., Modified TiO_2 photocatalyst for CO_2 photocatalytic reduction: An overview. Journal of CO_2 Utilization, 2017. 22: p. 15-32.

88. Pipornpong, W., R. Wanbayor, and V. Ruangpornvisuti, Adsorption CO_2 on the perfect and oxygen vacancy defect surfaces of anatase TiO_2 and its photocatalytic mechanism of conversion to CO. Applied Surface Science, 2011. 257: p. 10322–10328.

89. Adamczyk, K., et al., Real-Time Observation of Carbonic Acid Formation in Aqueous Solution. Science, 2009. 326(5960): p. 1690.

90. Núñez, O., et al., Unprecedented large solvent (H$_2$O vs D$_2$O) isotope effect in semiconductors photooxidation. Journal of Physical Organic Chemistry, 2019. 32(7): p. e3952.

จุฬาลงกรณ์มหาวิทยาลัย
CHULALONGKORN UNIVERSITY

APPENDIX

APPENDIX A

CALCULATION OF THE CRYSTALLITE SIZE

Calculation of the crystallite size by Debye-Scherrer equation. The crystallite size can be calculated from 2θ profile analysis, the half-height width of diffraction peak using the Debye-Scherrer equation.

From Scherrer equation: $$D = \frac{k\lambda}{\beta \cos\theta}$$ Eq. 55

Where

D = Crystallite size (Å)

k = Crystallite-shape factor (0.9)

λ = X-ray wavelength (1.5418 Å for CuKα)

β = X-ray diffraction broadening (radian)

θ = Observed peak angel (degree)

The X-ray diffraction broadening (β) can be obtained by using Warren's formula

Warren's equation: $$\beta^2 = \beta_M^2 - \beta_S^2$$ Eq. 56

$$\beta = \sqrt{\beta_M^2 - \beta_S^2}$$ Eq. 57

Where β_M = Measured peak width in radians at half peak height

β_S = Corresponding width of a standard material

Example: Calculation of the crystallite size of P25-TiO2.

Finding the half-weight width (101) diffraction peak at 25.3° from the XRD pattern

The half-weight width (101) diffraction peak;

β_M = 0.3959 degree

β_S = 0.0069 radian

The corresponding half-height width of the peak of P25-TiO2

β_S = 0.003836 radian

The pure width $$\beta = \sqrt{\beta_M^2 - \beta_S^2}$$

$$\beta = \sqrt{0.0069^2 - 0.0038^2}$$

Where λ = 1.54 Å

β = 0.00575 radian

θ = 12.65 degree

The crystallite size:

$$D = \frac{k\lambda}{\beta cos\theta}$$

$$D = \frac{(0.9)(1.54)}{(0.00575)cos(12.65)}$$

= 241.89 Å = 24.19 nm

APPENDIX B

CALCULATION OF WEIGHT COMPOSITION

The weight fraction of P25-TiO2 was calculated from the XRD pattern.

$$W_A = \frac{K_A A_A}{K_A A_A + K_B A_B + K_R} \qquad \text{Eq. 58}$$

$$W_B = \frac{K_B A_B}{K_A A_A + K_B A_B + K_R} \qquad \text{Eq. 59}$$

$$W_R = \frac{K_R}{K_A A_A + K_B A_B + K_R} \qquad \text{Eq. 60}$$

Where W_A = Weight fraction of anatase phase TiO2

W_B = Weight fraction of brookite phase TiO2

W_R = Weight fraction of rutile phase TiO2

A_A = The intensity of anatase peak

A_B = The intensity of brookite peak

A_R = The intensity of rutile peak

K_A = The coefficient factor of anatase (0.886)

K_B = The coefficient factor of brookite (2.721)

The phases of TiO2 can be calculated from the integrated intensities of the peak at $2\theta = 25.3°$ (anatase phase), the peak at $27.4°$ (rutile phase), and the peak at $30.6°$ (brookite phase). However, P25 catalyst consisted of anatase phase and rutile phase except for brookite phase.

Example: Calculation of the phase composition of P25-TiO2.

Where   The integrated intensities of anatase (A_A) = 2297.4

The integrated intensities of rutile (A_R) = 449.3

APPENDIX C

CALCULATION OF THE ENERGY BAND GAP FROM UV-VIS SPECTRA

From the UV light absorbance results at various wavelengths from 200 - 800 nm by UV - VIS Spectrophotometer. The absorption values at each wavelength were used for the energy bandgap calculation.

$$hv\alpha = const(hv - E_{bg})^n \hspace{4cm} \text{Eq. 61}$$

where h is Plank's constant = $4.13566743 \times 10^{-15}$ eV.s

v is Light frequency (1/s)

α is optical absorption coefficient

c is Speed of light = 299,792,458 m/s หรือ 2.997924×10^8 nm/s

n is Material constant of sample

E_{bg} is Energy band gap of catalyst (eV)

Example: The energy band gap calculation of P25 catalyst. From light absorption result at 400 nm wavelength, absorbance constant is 3.0996.

Then; λ = 400 nm, α = 0.186, h = $4.13566743 \times 10^{-15}$ eV.s, c = 299,792,458 m/s หรือ 2.997924×10^{17} nm/s and n = 1/2 for solid.

Therefore; $hv = hc / \lambda$

$hv = (4.13566743 \times 10^{-15} \text{ (eV.s)} \times 2.997924 \times 10^{17} \text{ (nm/s)}) / 400 \text{ (nm)}$

$hv = 3.0996$ eV

If;   K = α / const   ;assume const =1

$(K.hv)^2 = (0.186 \times 3.0996 \text{ eV})^2 = 0.3324$

Calculate the hv and $(K.hv)^2$ values at each wavelength, then the hv and $(K.hv)^2$ plot is used for energy band gap extrapolation. From Figure 33, the straight-line cut the X-axis presented the band gap energy of pure P25 is 3.27 eV.
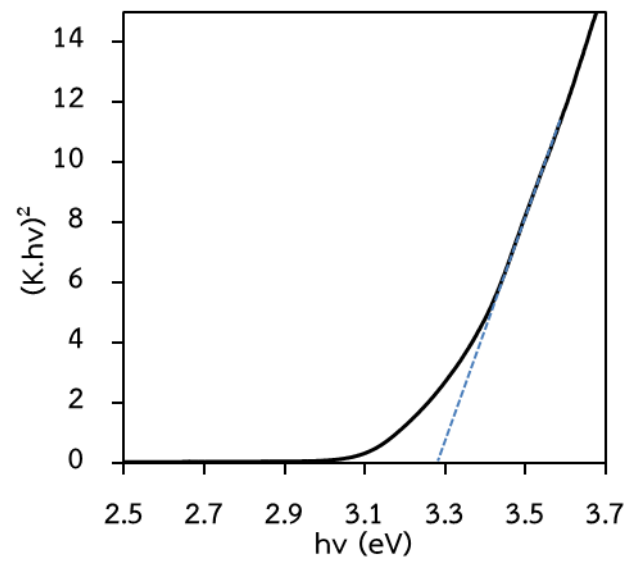
Figure 32 A plot between $(K.hv)^2$ vs. photon energy (hv) of P25

VITA

NAME   Duangthip Sattayamuk

DATE OF BIRTH   07 October 1995

PLACE OF BIRTH   Khonkaen

INSTITUTIONS ATTENDED   Chulalongkorn University

HOME ADDRESS   House No.4/20, Village No.7, Srijan Rd., Nai Muang Khon

                        kaen Sub-district, Muang Khon kaen, 40000, Thailand